Article

Modulation of inhibitory communication coordinates looking and reaching

https://doi.org/10.1038/s41586-022-04631-2

Received: 1 June 2021

Accepted: 11 March 2022

Published online: 20 April 2022

Check for updates

Maureen A. Hagan[1,2] & Bijan Pesaran[2]✉

Looking and reaching are controlled by different brain regions and are coordinated during natural behaviour[1]. Understanding how flexible, natural behaviours such as coordinated looking and reaching are controlled depends on understanding how neurons in different regions of the brain communicate[2]. Neural coherence in a gamma-frequency (40–90 Hz) band has been implicated in excitatory multiregional communication[3]. Inhibitory control mechanisms are also required to flexibly control behaviour[4], but little is known about how neurons in one region transiently suppress individual neurons in another to support behaviour. How neuronal firing in a sender region transiently suppresses firing in a receiver region remains poorly understood. Here we study inhibitory communication during a flexible, natural behaviour, termed gaze anchoring, in which saccades are transiently inhibited by coordinated reaches. During gaze anchoring, we found that neurons in the reach region of the posterior parietal cortex can inhibit neuronal firing in the parietal saccade region to suppress eye movements and improve reach accuracy. Suppression is transient, only present around the coordinated reach, and greatest when reach neurons fire spikes with respect to beta-frequency (15–25 Hz) activity, not gamma-frequency activity. Our work provides evidence in the activity of single neurons for a novel mechanism of inhibitory communication in which beta-frequency neural coherence transiently inhibits multiregional communication to flexibly coordinate natural behaviour.

The flexible control of behaviour depends on both excitatory and inhibitory mechanisms to route information flow between cortical regions[2]. Excitatory projection neurons can drive increases in activity in downstream regions by recruiting correlated[5] and coherent[3,6,7] temporal patterns of neural activity. Inhibitory control mechanisms also guide behaviour in the face of changing goals[4]. Whether and how increased firing of neurons in one cortical region can improve behavioural performance by suppressing firing in another cortical region remain poorly understood.

In primates, saccadic eye movements are naturally coordinated with arm movements to make accurate reach-and-grasp movements[8]. Subregions of the posterior parietal cortex are interconnected by excitatory projections across short white matter tracts called U-fibres[9,10]. Silencing neural firing in the parietal reach region (PRR) alters reaching and not saccades made alone, whereas silencing firing in the parietal saccade region (the lateral intraparietal area (area LIP)) alters saccades but not reaching[11,12]. Thus, communication between neurons in the PRR and neurons in area LIP may support coordinated visual behaviour.

In humans, behavioural inhibition improves reach performance through gaze anchoring[13]. Gaze is naturally 'anchored' to the target of an ongoing reach and new eye movements are inhibited, extending target foveation in time and improving reach accuracy. Neurons in the reach region guiding the reach may inhibit response selection in neurons in the saccade region that are responsible for the upcoming saccade. We therefore tested the activity of individual neurons in the PRR and the saccade region (area LIP) for evidence of inhibitory communication during gaze anchoring (Fig. 1a).

Inhibitory communication modulates gaze

We trained two non-human primates (*Macaca mulatta*) to perform a reach–saccade (RS) task, which should naturally elicit gaze anchoring, and a saccade-only (SS) task, which should not elicit gaze anchoring (Fig. 1b, Extended Data Fig. 1a; Methods). In the RS task, each monkey made a reach and saccade to a target, followed by a second saccade to a newly presented target. We presented the second saccade target at one of two spatial locations unexpectedly following reach completion (second target delay, 0–800 ms). In the SS task, each monkey made two saccades and no reach.

Both monkeys exhibited gaze anchoring naturally during the RS task (Methods). Second saccade reaction times (SSRTs) were significantly longer on RS peri-reach trials, when the second target appeared within 300 ms of the reach, than on RS post-reach trials, when the second target appeared 500–800 ms after reach completion (Fig. 1c). On peri-reach trials, reaching was significantly more accurate on trials with longer SSRTs, whereas on post-reach trials, the association between reach accuracy and SSRTs was inconsistent (Fig. 1d). SSRTs covaried with reach reaction times in the RS task, but not with the saccade reaction times in the SS task (Extended Data Fig. 1b–g). Thus, gaze anchoring occurs briefly during the RS peri-reach trials, and involves changes in reach and saccade movement performance.

[1]Department of Physiology and Neuroscience Program, Biomedicine Discovery Institute, Monash University, Clayton, VIC, Australia. [2]Center for Neural Science, New York University, New York, NY, USA. ✉e-mail: bijan@nyu.edu

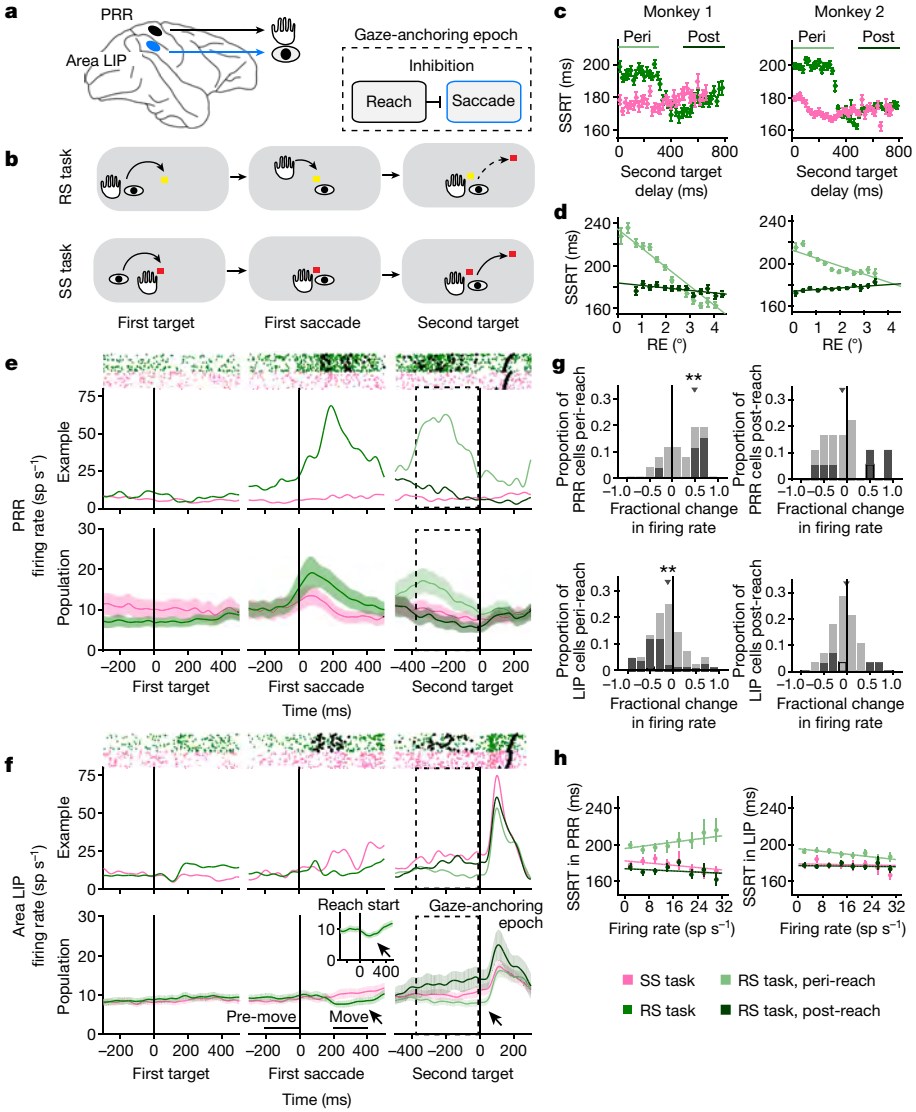

Fig. 1 | Coordinated behaviour and multiregional communication. **a**, Schematic. **b**, RS task and SS task, indicating the hand and eye positions for the task epoch. The dashed arrow in the RS task illustrates slowed saccade RT compared with the solid line in the SS task. **c**, SSRT against a second target delay for RS (green) and SS (pink) tasks. Peri-reach (light green) monkey 1 (M1) $P = 5 \times 10^{-62}$, $n = 8{,}140$ trials; monkey 2 (M2) $P = 5 \times 10^{-210}$, $n = 10{,}245$ trials. Post-reach (dark green) M1 $P = 1 \times 10^{-3}$, $n = 2{,}872$ trials; M2 $P = 0.54$, $n = 3{,}903$ trials; Student's *t*-test versus SS second target delay matched. **d**, SSRT against reach error (RE). Peri-reach (light green) M1 $R = -0.33$, slope = −17.8 ms per degree, $P = 1 \times 10^{-95}$; M2 $R = -0.15$, slope = −7.5 ms per degree, $P = 2 \times 10^{-33}$. Post-reach (dark green) M1 $R = -0.069$, slope = −2.3 ms per degree, $P = 2 \times 10^{-4}$; M2 $R = 0.061$, slope = 1.5 ms per degree, $P = 6 \times 10^{-5}$. All Student's *t*-test. *R* was measured using Pearson correlation. **e**, **f**, PRR (**e**) and LIP (**f**) firing rates. The inset shows reach onset aligned. The arrows indicate suppressed LIP firing. Mean fractional difference (MFD) = (RS − SS)/SS. RS task move versus pre-move MFD = −0.18, $P = 0.01$. SS task MFD = 0.01, $P = 0.10$. All signed-rank test. The dashed line is the gaze-anchoring epoch. Rasters: reach start (squares), reach stop (diamond) and second saccade (triangle). PRR firing did not significantly differ before the first target after controlling for initial eye–hand position (Methods; $P = 0.87$, permutation test). **g**, PRR population MFD (peri-reach MFD = 0.49, $P = 3.7 \times 10^{-4}$; post-reach MFD = −0.17, $P = 0.24$) and LIP population MFD (peri-reach MFD = −0.11, $P = 0.001$; post-reach MFD = −0.04, $P = 0.51$). All signed-rank test. The dark bars indicate significance of individual neurons ($P < 0.05$). The black outline denotes example cells. Downward triangles indicate the population MFD. **$P < 0.01$: the population MFD is significantly different from 0. **h**, Firing rates against SSRT. PRR (peri-reach Rho = 0.11, slope = 0.44 ms/(sp s^{-1}), $P = 0.001$; post-reach Rho = −0.06, $P = 0.35$; saccade Rho = −0.12, slope = −0.31 ms/(sp s^{-1}), $P = 0.004$) and LIP (peri-reach Rho = −0.10, slope = −0.37 ms/(sp s^{-1}), $P = 7 \times 10^{-7}$; post-reach Rho = −0.03, $P = 0.2$; saccade Rho = −0.02, $P = 0.54$). All permutation test. Rho was measured using Spearman's correlation. In **c**–**f** and **h**, data are shown as mean ± s.e.m.

Reaching inhibits saccade firing

To obtain evidence of inhibitory communication during gaze anchoring, we recorded from 120 spatially selective neurons in the parietal reach and saccade systems (PRR: 34 neurons, area LIP: 86 neurons; Methods; Extended Data Fig. 2). For each task, we presented the first movement target in the response field of a PRR neuron and the second target in the response field of an area LIP neuron. Consistent with a role in guiding the reach[14], PRR neurons fired more during coordinated reaches than during saccades made alone (Fig. 1e). Consistent with a role in guiding saccades[15], neurons in area LIP fired more when the second target was in the response field (Fig. 1f).

During the gaze-anchoring epoch, activity in area LIP was transiently suppressed during RS trials around the reach, starting at reach onset (Fig. 1f and inset). Comparing RS and SS trials, PRR neurons fired significantly more and area LIP neurons fired significantly less during gaze anchoring, but not 500 ms after the reach (Fig. 1g). Therefore, firing of PRR neurons may drive inhibition and suppress firing in area LIP during gaze anchoring.

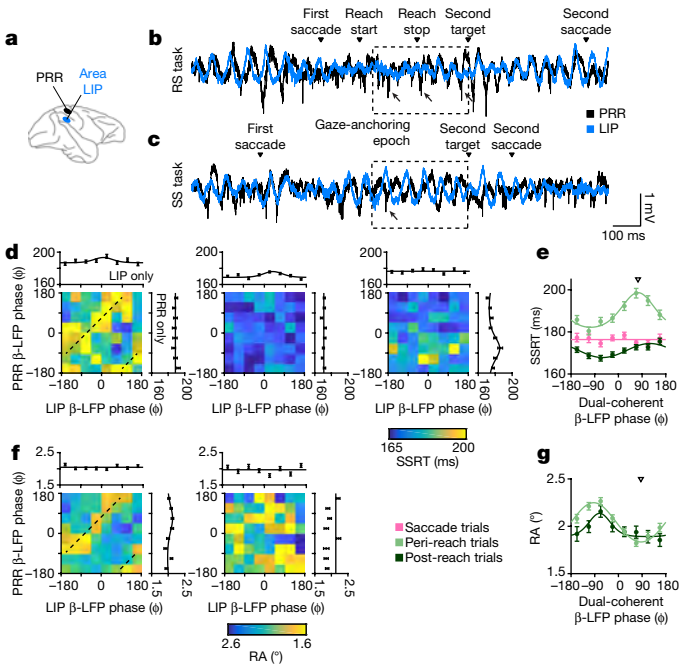

Fig. 2 | Behavioural performance and coherent neural dynamics. **a**, Schematic showing neural recordings. **b**, **c**, Voltage traces of RS task (**b**) and SS task (**c**) example trials. The dashed box indicates the gaze-anchoring epoch. The arrows indicate example spikes occurring at representative phases. **d**, Peri-reach (n = 4,814; left), post-reach (n = 2,116; middle) and saccade (n = 3,583; right) trials showing the mean beta-LFP phase in each cortical area and corresponding SSRT (colour scale). Marginals show SSRT against the beta-LFP phase in each area alone (SSRT versus PRR only: peri-reach $P = 0.09$; post-reach $P = 0.40$; saccade $P = 3.7 \times 10^{-12}$. SSRT versus LIP only: peri-reach $P = 0.025$; post-reach $P = 6.4 \times 10^{-6}$; saccade $P = 0.12$). **e**, SSRT against the dual-coherent beta-LFP phase for each trial type (peri-reach $P = 2.2 \times 10^{-16}$; post-reach $P = 1.40 \times 10^{-5}$, preferred phase = 120°; saccade $P = 0.5$). The solid lines present SSRT fitted by a von Mises function. **f**, Peri-reach and post-reach trials showing the mean beta-LFP phase in each cortical area and the corresponding RE (colour scale). Marginals show the RE against the mean PRR spike beta-LFP phase in each area alone (PRR only: peri-reach $P = 6.4 \times 10^{-3}$, variation in RE: 0.15°, 7% fractional change (ΔRE/mean(RE)); post-reach $P = 1$. LIP only: peri-reach $P = 0.36$; post-reach $P = 0.2$). **g**, RE against the dual-coherent beta-LFP phase for each trial type (peri-reach variation in RE = 0.45°, 22% fractional change, $P = 0$; post-reach variation in RE = 0.25°, 12% fractional change, $P = 4.2 \times 10^{-3}$); conventions as in **e**. The downward triangles present the mean of the von Mises fit dual-coherent beta-LFP phase on peri-reach trials at the maximum SSRT (**e**) or the minimum RE (**g**). The dashed lines in **d** and **f** indicate the dual-coherent phase shown by the downward triangles in **e** and **g**. All P values report the likelihood-ratio test. In **d**–**g**, data are shown as mean ± s.e.m.

Changes in area LIP and PRR firing rate reflected gaze anchoring. PRR neurons fired more and area LIP neurons fired less on peri-reach trials with longer SSRTs, but not with shorter SSRTs (Fig. 1h). This inverse relationship was transient and task-dependent: neural gaze-anchoring effects were specific to coordinated movements and were not observed at other times. Firing of a subset of simultaneously recorded area LIP and PRR neurons was negatively correlated during gaze-anchoring trials, but was positively correlated during other trials (32 pairs, peri-reach trial $R = -0.07$, $P = 0.02$; post-reach trial $R = 0.2$, $P = 5 \times 10^{-6}$; saccade trial $R = 0.08$, $P = 0.01$; Spearman's correlation).

Beta coherence modulates gaze anchoring

Correlations in firing rate suggest that gaze anchoring is due to neurons in the PRR communicating with neurons in area LIP. If so, behavioural performance should vary with reach-to-saccade communication. We therefore analysed how performance varies with neural activity on peri-reach trials compared with post-reach and saccade trials.

We sought to find out how one region might exert a transient, task-dependent inhibitory or suppressive effect on another. Neuronal coherence is the correlated timing of neural activity across groups of neurons measured by the phase of local field potential (LFP) activity in specific frequency bands[16]. As the strength of neural interactions depends on the timing of neuronal activity with respect to neural excitability, multiregional communication may depend on the phase of neural coherence. Neural activity in the beta-frequency band reflects suppression of movement initiation[14,17,18], motor processing[19,20], top-down feedback[21,22] and multiregional integration[23–25] and may support inhibitory communication. If so, inhibition between the PRR and area LIP, and behavioural performance, should covary with spike timing with respect to the phase of beta-frequency activity in the PRR and area LIP.

We conducted 151 experimental sessions with PRR spiking recorded simultaneously with LFPs in the PRR and area LIP (Fig. 2a). In the RS task, LFP activity in area LIP and the PRR synchronized around the reach, with spiking in the PRR tending to occur at a particular phase of beta-frequency LFP activity in both areas (Fig. 2b). On SS trials, spiking in the PRR tended to occur at a different phase of beta-frequency LFP activity in both areas (Fig. 2c, Extended Data Fig. 3).

We next investigated whether the beta-frequency spike-LFP phase predicted changes in coordinated behaviour (Methods). The PRR-only phase did not predict SSRTs on peri-reach or post-reach trials, but did predict SSRTs on saccade trials, whereas the LIP-only phase was inconsistent with gaze anchoring and most strongly predicted SSRTs on post-reach trials (Fig. 2d). These data show that PRR spiking with respect to the single-region phase does not predict variations in performance at times when reach-to-saccade communication is expected, during peri-reach trials.

Recent work links multiregional communication to spike timing with respect to the phase of beta-frequency coherence in both regions, termed dual coherence[26]. Multiregional communication may therefore occur when beta-frequency coherence has a consistent phase difference across the reach-and-saccade system and may be suppressed at other times.

We computed the dual-coherent phase for each trial (Methods). Variations in performance with the dual-coherent phase were consistent with gaze anchoring. On peri-reach trials, SSRTs significantly varied with the dual-coherent phase and were slowest on trials with a preferred dual-coherent phase of approximately 75° (Fig. 2e; Methods). SSRTs did not significantly vary with the dual-coherent phase on saccade trials (Fig. 2e). SSRTs on peri-reach trials with non-preferred dual-coherent phases did not increase compared with saccade trials (SSRT peri-reach versus saccade trials at −112°, $P = 0.25$, permutation test). SSRTs significantly varied with the dual-coherent phase on post-reach trials (Fig. 2e), but slowing of the post-reach SSRT (6 ms) was smaller than slowing of the peri-reach SSRT (17 ms).

These data demonstrate that the relationship between slowing of the SSRT and dual-coherent PRR spike timing is consistent with reach-to-saccade communication on reach trials and not saccade trials.

We analysed whether PRR spike timing also predicted reach accuracy. PRR spiking with the LIP-only phase did not predict improved reach accuracy, whereas PRR spiking with the PRR-only phase predicted reach accuracy on peri-reach but not post-reach trials, albeit weakly (Fig. 2f). By contrast, reach accuracy significantly and strongly depended on the dual-coherent phase (Fig. 2g). On post-reach trials, reach accuracy also significantly depended on the dual-coherent phase, albeit more weakly than on peri-reach trials (Fig. 2g).

Variations of reach accuracy and SSRT with the dual-coherent phase were consistent with a common underlying mechanism of communication. On peri-reach trials, reaches were most accurate and SSRT was slowest at a similar dual-coherent phase (reach accuracy: 91°, SSRT: 75°). Variations with a single-region phase were not consistent with a common underlying mechanism.

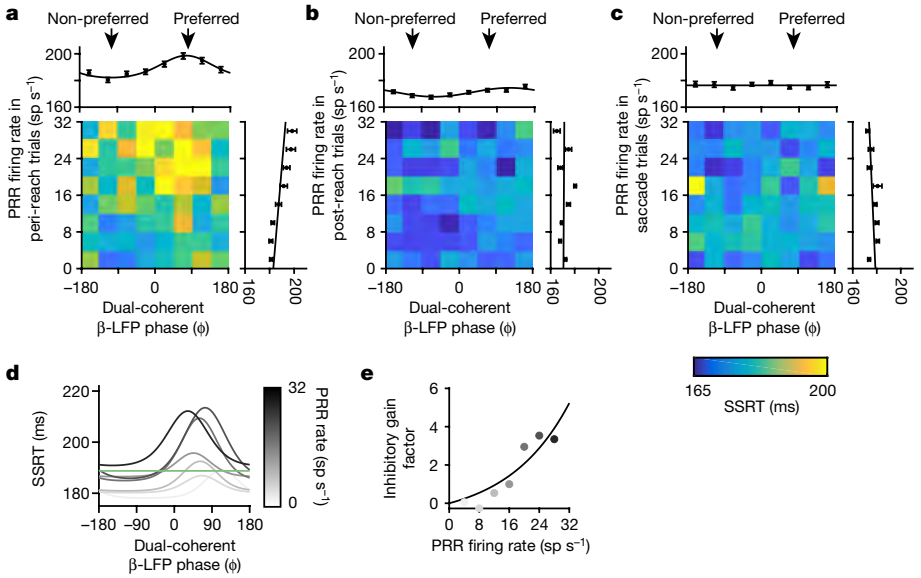

Fig. 3 | State-dependent inhibitory communication. a–**c**, Peri-reach (**a**), post-reach (**b**) and saccade (**c**) trials showing PRR firing rate and the dual-coherent beta-LFP phase and their relationship to SSRT (colour scale). The marginals show SSRT against PRR firing rate or the dual-coherent beta-LFP phase alone. Peri-reach preferred $R = 0.15$, $P = 9 \times 10^{-4}$; non-preferred $R = 0.01$, $P = 0.82$. Post-reach preferred $R = 0.01$, $P = 0.85$. Saccade preferred $R = -0.02$, $P = 0.81$. Data are shown as mean ± s.e.m. **d**, Peri-reach modulation state functions fit to PRR firing rate bins. The green line indicates the mean SSRT. **e**, Gain factor function fit to the scaled peaks of the modulation state functions presented in **d** for each PRR firing rate bin. Adjusted $R^2 = 0.76$. R was measured by Pearson correlation. Sample size reported in Fig. 2.

Parametrically fitting SSRT and reach accuracy to phase trial-by-trial showed that the dual-coherent phase had a greater likelihood and less generalization error than the single-region phase (Methods; Extended Data Fig. 4). Non-parametric analysis of SSRT, reach accuracy and phase trial-by-trial provided convergent evidence consistent with the absence of reach-to-saccade communication on saccade trials and more communication on peri-reach trials than on post-reach trials.

Dual coherence on peri-reach trials may be driven by the evoked LFP phase change at reach onset. However, reach-onset-aligned dual coherence predicted slowing of the SSRT even after explicitly subtracting the evoked LFP response (Extended Data Fig. 5).

Additional analyses emphasized PRR spike timing with respect to the beta-frequency dual-coherent phase. Variations in the phase of the beta-frequency LFP phase alone did not predict gaze-anchoring-related slowing of the SSRT (Extended Data Fig. 6). Beta-frequency coherence has a period of 50 ms, which implies that spike timing changes every quarter-cycle, for example, 12.5 ms. We therefore jittered PRR spike times on each trial (Methods). The PRR-spike dual-coherent phase on peri-reach trials predicted SSRT only when jittering by less than 10 ms (Extended Data Fig. 7).

Effects were specific to dual coherence in the beta frequency (20 Hz), but not in the gamma frequency (40 Hz). The gamma-frequency dual-coherent phase had a small but significant effect on SSRT on peri-reach trials that was significantly smaller than for the beta-frequency dual-coherent phase (Extended Data Fig. 8).

As the spike rate in area LIP predicted slowing of the SSRT, we asked whether the spike timing in area LIP with respect to the dual-coherent phase also predicted slowing of the SSRT. Whereas the LIP-spike beta-frequency dual-coherent phase had a small but significant correlation with the SSRT on peri-reach trials, the SSRT varied with the PRR spike dual-coherent phase significantly more than with the LIP spike dual-coherent phase (Extended Data Fig. 9).

Consequently, spike timing in the PRR may drive behavioural inhibition during gaze anchoring to slow the SSRT and improve reach accuracy with respect to the beta-frequency dual-coherent phase compared with the single-region beta-frequency phase, LFP coherence phase, gamma-frequency coherence and LIP spike timing.

A reach-to-saccade communication channel

As spiking in the PRR does not generally guide saccades, PRR spiking may suppress saccades depending on modulation of a reach-to-saccade communication channel. According to this channel modulation hypothesis, when the channel opens, the SSRT lengthens because firing in the PRR is more effective at suppressing saccades. When the channel closes, the SSRT shortens because firing in the PRR is less effective at suppressing saccades. We analysed PRR spiking and SSRTs for evidence of state-dependent reach-to-saccade communication.

Firing in the PRR covaried with gaze-anchoring-related increases in SSRTs on trials when the dual-coherent phase was preferred, but not when the dual-coherent phase was non-preferred (Fig. 3a), and not during post-reach or saccade trials (Fig. 3b, c). Thus, the SSRT may depend on a state-dependent gain in which input drive from the PRR is gain-modulated by channel state, for example, the dual-coherent phase. During certain modulation states, large changes in PRR activity are compressed with small gain and the channel is effectively closed. During other modulation states, the same changes in PRR activity can lead to changes with larger gain and the channel is effectively open.

To better understand channel gain and modulation, we divided trials based on the level of PRR firing and fit SSRT with the dual-coherent phase (Fig. 3d). This analysis revealed a gain mechanism. As the firing rate in the PRR increased, the SSRT slowed more on trials when the channel was more open. The gain factor revealed a non-linear slowing of the SSRT with PRR activity (Fig. 3e). State-dependent non-linear gain underlies how the channel can be more open or closed.

Neurons in the PRR fired the same number of spikes across trials independent of the dual-coherent phase during gaze anchoring (Extended Data Fig. 10). This suggests that the firing rate in the PRR is not modulated by channel state and is consistent with the role of a sender in this circuit.

Channel modulation predicts suppression

The channel modulation model explains how gaze anchoring is controlled by reach-to-saccade communication according to PRR firing, dual-coherent phase and SSRT. The model also makes testable predictions about how the saccade system in general, and firing in area LIP in particular, should depend on PRR firing and dual-coherent phase. Figure 4a illustrates the model and predictions. According to the model, sender activity in the PRR acts as input to the communication channel. The channel transforms the PRR input to suppress activity in area LIP from the pre-move epoch to the move epoch, and saccade behaviour, according to two dissociable components: a 'gain' function models the inhibitory gain for the PRR firing on that trial, and a 'modulation' state function models the state of the dual-coherent phase on that trial (Methods).

We modelled and fit the input gain and the modulation state using saccade behaviour without directly observing neural activity in the saccade system. Input gain and modulation state were observed and fit using PRR firing and the dual-coherent phase from Fig. 3. Moreover, as in the model area LIP reflects the output of the communication

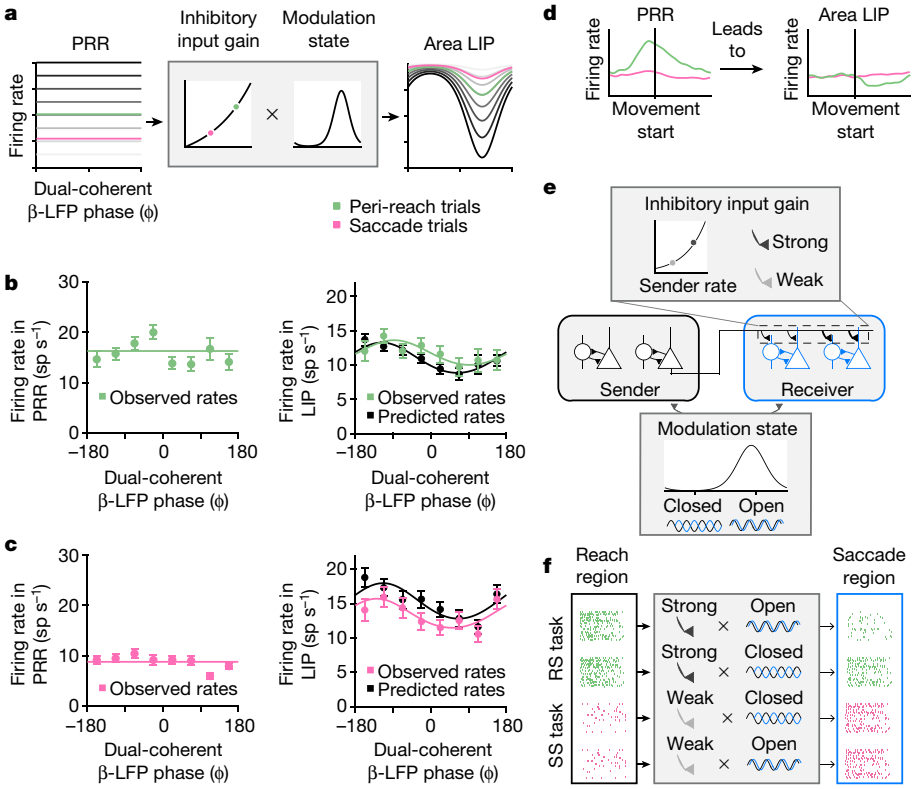

Fig. 4 | Channel modulation predicts LIP firing rates. a, Channel modulation model takes inputs as the PRR firing rate and the dual-coherent beta-LFP phase. The PRR rate determines the input gain and the dual-coherent beta-LFP phase determines the modulate state. The product of these two functions makes a prediction about the LIP firing rate. **b**, Simultaneously observed PRR and LIP firing rates on peri-reach trials (n = 1,188; light green) and the predicted LIP firing rates from the model (black) against the dual-coherent beta-LFP phase. The channel modulation model had the lowest mean squared error: channel modulation model = 175; gain only = 177; modulation only = 185; regression = 247. **c**, Simultaneously observed PRR and LIP firing rates on saccade trials (n = 942; pink) and the predicted LIP firing rates from the model (black) against the dual-coherent beta-LFP phase. The channel modulation model had the lowest mean squared error: channel modulation model = 137; gain only = 138; modulation only = 285; regression = 232. In **b** and **c**, data are shown as mean ± s.e.m. **d**, Schematic showing activity in the PRR leads to suppressed activity in the area LIP. **e**, This inhibition is predicted by the channel modulation model, which consists of an input gain function that ranges from weak to strong and a modulation state function that ranges between open and closed. **f**, High sender activity during the RS task may lead to strong inhibitory input, which on 'open'-state trials leads to suppression in the saccade area. Whereas low reach activity during the SS task means that the inhibitory input gain is weak and does not drive suppression regardless of the modulation state.

channel that guides saccade behaviour, the model predicts activity in area LIP. Firing in area LIP should be suppressed from the move epoch during the RS task but not during the SS task. The suppression should follow the strength of PRR firing, which determines the gain, and the dual-coherent phase, which determines the modulation state. The model never observes activity in area LIP during the move epoch that reveals gaze anchoring (Methods).

To test the model, we analysed simultaneously recorded firing of PRR neurons, area LIP neurons, SSRT and dual-coherent phase (32 spatially selective PRR–LIP neuron pairs; 88 spike–spike–LFP–LFP sessions; Methods). We measured PRR firing rates and the dual-coherent phase and used the model to predict simultaneously recorded LIP firing on each trial. Although PRR firing did not vary with the dual-coherent phase, in the experimental data, firing in area LIP significantly covaried with the dual-coherent phase (Fig. 4b, green) and was maximally suppressed at the same preferred phase angle as the SSRT variations with the dual-coherent phase (minimum rate at 92°, von Mises fit). These features were predicted by the model from the observed PRR firing and dual-coherent phase (Fig. 4b, black).

We evaluated the contributions of the input gain, modulation state and their combination using reduced models (Methods). The channel modulation model best predicted the observed firing rates in area LIP during the RS task. Removing the gain term degraded the prediction more than removing the modulation term. A regression fit using simultaneous recordings of neuron firing in the PRR and area LIP performed worse. At lower PPR firing rates, as in the SS task, the model predicted weak modulation of LIP firing rates (Fig. 4a). Firing rates in area LIP in the SS task were also predicted from PRR firing and the dual-coherent phase on each trial (Fig. 4c). The modelling results suggest that PRR firing can influence area LIP firing during gaze anchoring to coordinate looking and reaching.

Discussion

Here we investigated the mechanisms of inhibitory communication during eye–hand coordination in the activity of individual neurons[27,28]. Behavioural task design allowed us to decompose a naturally expressed behaviour, gaze anchoring, into components to establish that multi-regional communication features dissociable gain and modulation components. Gaze anchoring ensured that communication went from the reach system to the saccade system. Activity in area LIP related to the second saccade could not be responsible for signals in the PRR that improve reach accuracy because we presented the second saccade target after the reach and placed the two saccade targets such that neural response fields in area LIP did not spatially overlap. As gaze anchoring is naturally expressed, confounding influences due to training are also relatively absent.

Our results suggest that beta-frequency neural coherence modulates how much reach-related firing suppresses saccade-related firing (Fig. 4e, f). When reach activity is high, input gain is strong and the saccade region is more or less suppressed depending on the modulation

state. When reach activity is low, input gain is weak and the saccade region does not depend on the modulation state (Fig. 4g).

We have shown that inhibitory communication involves beta coherence and not gamma coherence[29]. Slower saccades and accurate reaches occur with a relative phase of approximately 75°. As beta-frequency (20 Hz) activity has a period of 50 ms, 75° corresponds to an approximately 10-ms time difference and is consistent with a time delay due to the latency for presynaptic spike propagation in the PRR across U-fibres to area LIP, as well as postsynaptic hyperpolarization in area LIP due to inhibitory GABA synapses. This result dissociates the excitability of spiking in a given brain region from behavioural effects of spiking across multiple brain regions. Although PRR spikes tend to occur for a specific combination of beta-frequency phases in the PRR and area LIP, the beta-frequency phase may reflect PRR excitability (Extended Data Fig. 3). However, as the impact of PRR spikes to slow saccades for accurate reaching varies with the relative phase and not a specific combination of phases (Fig. 2), multiregional communication depends on a time delay. The effect of PRR spiking on area LIP is greatest when PRR beta coherence differs from area LIP beta coherence with an approximately 10-ms time delay.

Previous work has also linked beta coherence to GABAergic activity experimentally[30–33] and through modelling[30]. Our results suggest that beta coherence may specifically engage feedforward inhibition by suppressing synaptic influences from the PRR on area LIP across an inhibitory feedforward pathway[34]. Note that our results do not imply that LFP activity exerts causal influences on brain function. Interacting populations of neurons may instead exert causal influences that are measured by a relative LFP phase.

Our work constrains theoretical explanations for how multiregional neural population dynamics exert causal effects on behaviour. We have shown that the mechanism of modulation depends on spike timing at 5–10-ms timescales. Neural population dynamics at slower 50–100-ms timescales may explain the gain component but not the modulation component. Therefore, relatively fast firing dynamics are needed to explain the mechanisms of behaviourally relevant communication.

Inhibitory control mechanisms have been implicated in flexible, coordinated behaviour[17,35,36], visual attention[25,37] and dual-task performance[38]. We have shown that an increase in the reach-related firing of individual neurons in the PRR is associated with net suppression of firing by individual neurons in area LIP, and the slowed initiation of saccades to visual targets presented unexpectedly at different spatial locations. Net suppression and slowed saccade initiation is consistent with suppressed attentional selection throughout area LIP. Consequently, beta-frequency modulation may allow the reach system to transiently suppress attentional selection in the saccade system. Beta-frequency multiregional communication may reflect a general mechanism of inhibitory cognitive control necessary for flexible behaviour.

Online content

Any methods, additional references, Nature Research reporting summaries, source data, extended data, supplementary information, acknowledgements, peer review information; details of author contributions and competing interests; and statements of data and code availability are available at https://doi.org/10.1038/s41586-022-04631-2.

1. Milner, D. & Goodale, M. *The Visual Brain in Action* (Oxford Univ. Press, 2006).
2. Hahn, G., Ponce-Alvarez, A., Deco, G., Aertsen, A. & Kumar, A. Portraits of communication in neuronal networks. *Nat. Rev. Neurosci.* **20**, 117–127 (2019).
3. Buschman, T. J. & Miller, E. K. Top-down versus bottom-up control of attention in the prefrontal and posterior parietal cortices. *Science* **315**, 1860–1862 (2007).
4. Anderson, M. C. & Weaver, C. In *Encyclopedia of Neuroscience* (ed. Squire, L. R.) 153–163 (Academic Press, 2009).
5. Semedo, J. D., Zandvakili, A., Machens, C. K., Yu, B. M. & Kohn, A. Cortical areas interact through a communication subspace. *Neuron* **102**, 249–259.e4 (2019).
6. Gregoriou, G. G., Gotts, S. J., Zhou, H. & Desimone, R. High-frequency, long-range coupling between prefrontal and visual cortex during attention. *Science* **324**, 1207–1210 (2009).
7. Pesaran, B., Nelson, M. J. & Andersen, R. A. Free choice activates a decision circuit between frontal and parietal cortex. *Nature* **453**, 406–409 (2008).
8. Abrams, R. A., Meyer, D. E. & Kornblum, S. Eye-hand coordination: oculomotor control in rapid aimed limb movements. *J. Exp. Psychol. Hum. Percept. Perform.* **16**, 248–267 (1990).
9. Catani, M. et al. Short parietal lobe connections of the human and monkey brain. *Cortex* **97**, 339–357 (2017).
10. Lewis, J. W. & van Essen, D. C. Corticocortical connections of visual, sensorimotor, and multimodal processing areas in the parietal lobe of the macaque monkey. *J. Comp. Neurol.* **428**, 112–137 (2000).
11. Kubanek, J., Li, J. M. & Snyder, L. H. Motor role of parietal cortex in a monkey model of hemispatial neglect. *Proc. Natl Acad. Sci. USA* **112**, E2067–E2072 (2015).
12. Hwang, E. J., Hauschild, M., Wilke, M. & Andersen, R. A. Inactivation of the parietal reach region causes optic ataxia, impairing reaches but not saccades. *Neuron* **76**, 1021–1029 (2012).
13. Neggers, S. F. & Bekkering, H. Ocular gaze is anchored to the target of an ongoing pointing movement. *J. Neurophysiol.* **83**, 639–651 (2000).
14. Hagan, M. A., Dean, H. L. & Pesaran, B. Spike-field activity in parietal area LIP during coordinated reach and saccade movements. *J. Neurophysiol.* **107**, 1275–1290 (2012).
15. Barash, S., Bracewell, R. M., Fogassi, L., Gnadt, J. W. & Andersen, R. A. Saccade-related activity in the lateral intraparietal area. II. Spatial properties. *J. Neurophysiol.* **66**, 1109–1124 (1991).
16. Pesaran, B. et al. Investigating large-scale brain dynamics using field potential recordings: analysis and interpretation. *Nat. Neurosci.* **21**, 903–919 (2018).
17. Dean, H. L., Hagan, M. A. & Pesaran, B. Only coherent spiking in posterior parietal cortex coordinates looking and reaching. *Neuron* **73**, 829–841 (2012).
18. Pape, A.-A. & Siegel, M. Motor cortex activity predicts response alternation during sensorimotor decisions. *Nat. Commun.* **7**, 13098 (2016).
19. Kristeva, R., Patino, L. & Omlor, W. Beta-range cortical motor spectral power and corticomuscular coherence as a mechanism for effective corticospinal interaction during steady-state motor output. *NeuroImage* **36**, 785–792 (2007).
20. Chung, J. W., Ofori, E., Misra, G., Hess, C. W. & Vaillancourt, D. E. Beta-band activity and connectivity in sensorimotor and parietal cortex are important for accurate motor performance. *NeuroImage* **144**, 164–173 (2017).
21. Brovelli, A. et al. Beta oscillations in a large-scale sensorimotor cortical network: directional influences revealed by Granger causality. *Proc. Natl Acad. Sci. USA* **101**, 9849–9854 (2004).
22. Lee, J. H., Whittington, M. A. & Kopell, N. J. Top-down beta rhythms support selective attention via interlaminar interaction: a model. *PLoS Comput. Biol.* **9**, e1003164 (2013).
23. Tan, H., Wade, C. & Brown, P. Post-movement beta activity in sensorimotor cortex indexes confidence in the estimations from internal models. *J. Neurosci.* **36**, 1516–1528 (2016).
24. Hawellek, D. J., Wong, Y. T. & Pesaran, B. Temporal coding of reward-guided choice in the posterior parietal cortex. *Proc. Natl Acad. Sci. USA* **113**, 13492–13497 (2016).
25. Fiebelkorn, I. C., Pinsk, M. A. & Kastner, S. A dynamic interplay within the frontoparietal network underlies rhythmic spatial attention. *Neuron* **99**, 842–853.e8 (2018).
26. Wong, Y. T., Fabiszak, M. M., Novikov, Y., Daw, N. D. & Pesaran, B. Coherent neuronal ensembles are rapidly recruited when making a look-reach decision. *Nat. Neurosci.* **19**, 327–334 (2016).
27. Pesaran, B., Hagan, M., Qiao, S. & Shewcraft, R. Multiregional communication and the channel modulation hypothesis. *Curr. Opin. Neurobiol.* **66**, 250–257 (2020).
28. Krakauer, J. W., Ghazanfar, A. A., Gomez-Marin, A., MacIver, M. A. & Poeppel, D. Neuroscience needs behavior: correcting a reductionist bias. *Neuron* **93**, 480–490 (2017).
29. Bastos, A. M. et al. Visual areas exert feedforward and feedback influences through distinct frequency channels. *Neuron* **85**, 390–401 (2015).
30. Jensen, O. et al. On the human sensorimotor-cortex beta rhythm: sources and modeling. *NeuroImage* **26**, 347–355 (2005).
31. Yamawaki, N., Stanford, I. M., Hall, S. D. & Woodhall, G. L. Pharmacologically induced and stimulus evoked rhythmic neuronal oscillatory activity in the primary motor cortex in vitro. *Neuroscience* **151**, 386–395 (2008).
32. Hall, S. D. et al. The role of GABAergic modulation in motor function related neuronal network activity. *NeuroImage* **56**, 1506–1510 (2011).
33. Baumgarten, T. J. et al. Beta peak frequencies at rest correlate with endogenous GABA /Cr concentrations in sensorimotor cortex areas. *PLoS ONE* **11**, e0156829 (2016).
34. Pouille, F. & Scanziani, M. Enforcement of temporal fidelity in pyramidal cells by somatic feed-forward inhibition. *Science* **293**, 1159–1163 (2001).
35. Rogal, L. & Fischer, B. Eye-hand-coordination: a model for computing reaction times in a visually guided reach task. *Biol. Cybern.* **55**, 263–273 (1986).
36. Hoff, B. & Arbib, M. A. Models of trajectory formation and temporal interaction of reach and grasp. *J. Mot. Behav.* **25**, 175–192 (1993).
37. Wimmer, R. D. et al. Thalamic control of sensory selection in divided attention. *Nature* **526**, 705–709 (2015).
38. Watanabe, K. & Funahashi, S. Neural mechanisms of dual-task interference and cognitive capacity limitation in the prefrontal cortex. *Nat. Neurosci.* **17**, 601–611 (2014).

Methods

Experimental preparation

Two male rhesus monkeys (*M. mulatta*) participated in the experiments (monkey 1, 9.5 kg and monkey 2, 6.5 kg). Animals were not assigned to groups, so there was no randomization or blinding to group. Each animal was first implanted with an MRI-compatible head cap under general anaesthesia. A structural MRI was obtained with 0.5 mm isotropic voxels and was used to guide the placement of a recording chamber over the posterior parietal cortex of the hemisphere contralateral to the reaching arm (monkey 1: right reaching arm and left hemisphere; monkey 2: left reaching arm and right hemisphere) in a second surgical procedure. Chamber placement and electrode recording sites were registered to the structural MRI to within 1 mm (BrainSight, Rogue Research). The structural MRIs were also used to estimate recording locations for area LIP and PRR (see Extended Data Fig. 2). All surgical and animal care procedures were done in accordance with the National Institutes of Health guidelines and were approved by the New York University Animal Care and Use Committee.

Behavioural experiments

Experimental hardware and software. Eye position was monitored with a video-based eye tracker (I-Scan). Visual stimuli were generated using an array of tristate light-emitting diodes (LEDs; Kingbright) situated directly behind a touch screen (ELO Touchsystems). The LEDs formed a grid with points spaced at 10° intervals. The use of LEDs to present visual stimuli allowed for precise temporal control of stimulus onset and offset. LEDs also ensured that there was no source of background illumination that could influence reach accuracy. Reach accuracy was measured as the reach error by calculating the Euclidean distance between the target LED and the position of the hand on the touch screen. Trials for which the hand position at reach completion was more than 5° from the target were excluded from further analysis. The visual stimuli were controlled via custom LabVIEW (v8.5, National Instruments) software executed on a real-time embedded system (NI PXI-8184, National Instruments).

Experimental design. Each monkey first performed a centre-out saccade task to map the spatial saccade response fields of neurons. On a subset of sessions, each monkey also performed a centre-out reach-and-saccade task to map spatial reach response fields of neurons. Each monkey then performed the reach-and-saccade double-step task (RS trials) or the saccade–saccade double-step task (SS trials) to study gaze anchoring in a manner that was consistent with natural behaviour. On a subset of catch trials (percent of trials: monkey 1: 15% (13–18%), monkey 2: 17% (15–23%), median (interquartile range)), subjects performed only the first step of the double-step tasks with no second target to suppress anticipation. All RS, SS and catch trial conditions were randomly interleaved.

Centre-out tasks. At the start of each trial, ocular fixation and manual touch were instructed by a green target and a red target, placed centrally side by side. The green target indicated the start position for the hand touch, and the red target indicated the start position for the eye. The subject fixated while touching the screen for a variable baseline period of 500–800 ms. In the centre-out saccade task, a red saccade target would appear in the periphery. In the centre-out reach-and-saccade task, a yellow saccade target would appear in the periphery. There were eight possible target locations in each task. Each monkey then maintained fixation and touch for a variable delay period of 1,000–1,500 ms. After the delay period, the central fixation target would extinguish, cueing each monkey to saccade to the target location while maintaining hand position at the initial touch position for the centre-out saccade task, or the reach-and-saccade to the target location for the centre-out reach-and-saccade task.

Reach-and-saccade double-step task (RS task). Initial fixation and touch were again instructed by a red target and a green target, respectively. The initial position was placed 10° to the left (monkey 1) or the right (monkey 2) of the central target on the horizontal axis, ipsilateral to the recording chamber. Each monkey touched and fixated for a variable baseline of period of 500–800 ms, after which a yellow target would appear at the central location. After a variable delay of 1,000–1,500 ms, the initial touch and fixation were extinguished cueing a reach and saccade to the yellow target. The second saccade target was presented after the reach was completed after an interval of 10–800 ms. The second saccade target was a red LED cueing a saccade alone, presented after the reach was completed after an interval of 10–800 ms and placed either in the response field of the area LIP neuron under study or at an alternative target location also positioned in the contralateral visual field but outside the response field.

Saccade–saccade double-step task (SS task). Initial fixation was cued by a red target 10° away horizontally from the central target and the initial touch was cued by a green target at the central target location. The first saccade target also appeared at the central location, cuing the first saccade towards the hand. As a result, the hand–eye position before the second saccade was identical to that during the RS task. After the baseline period, a red target would appear at the central location. After a variable delay of 500–800 ms, the initial fixation target was extinguished cueing a saccade alone to the central target. As in the RS task, the second target was a red LED cueing a saccade alone. The second target was presented 10–1,000 ms after the first saccade.

We matched the time interval from the first saccade to presentation of the second saccade target across the SS and RS tasks. Monkeys were not rewarded for making fast or slow eye movements in either task. Overall, visual and oculomotor spatial and temporal contingencies were matched between the two tasks so that the tasks were naturalistic, did not require dedicated training and differed according to whether the subject made a reach. In pilot experiments, we also observed that presenting the second saccade target after the first saccade and during the reach resulted in changes in coordinated visual behaviour that altered the timing of the coordinated reach and saccade and led to inconsistent task performance. This was probably due to confusion about the cues, and their interference with ongoing visual processes needed to guide the first movement, such as attention. As presenting second saccade targets during the reach would require training to ensure consistent task performance, we only studied presentations of the second saccade target after the reach was completed, which both monkeys could perform successfully without the need for additional training.

Behavioural database. We collected a database of trials from each monkey for each task (monkey 1: 10,324 RS task, 8,372 SS task; monkey 2: 12,840 RS task, 8,452 SS task) across 10 task conditions that were randomly interleaved. This allowed us to analyse the relationship between the latency of the second saccade and the variables of the two tasks in sufficient detail to identify and test multiregional communication. Trials in which saccade and reach reaction times, for both steps, were not within a 100–500-ms window were discarded. This ensures that on all trials analysed, the subject was neither anticipating nor being inattentive to the targets.

SSRT versus second target delay. We compared second saccade reaction time to second target delay from the first saccade (both tasks), second target delay from reach completion, reach reaction time, reach duration, and reach reaction time minus saccade reaction time for the first step (RS task only). For presentation, we mapped the independent variable in 10-ms bins on a graph (Fig. 1c). Each bin needed a minimum of 20 trials to be included in the analysis, although the average number of trials was usually much greater (monkey 1: RS task, 198 ± 130

mean ± s.d. (118–195 interdecile range); SS task, 162 ± 29 mean ± s.d. (75–387 interdecile range); monkey 2: RS task, 263 ± 178 mean ± s.d. (29–220 interdecile range); SS task, 158 ± 63 mean ± s.d. (49–493 interdecile range)).

SSRT versus reach accuracy. We measured the association between the second saccade reaction time and the accuracy of the reach by performing linear regression and reporting the slope, statistical significance and correlation coefficient separately for peri-reach trials and post-reach trials (Fig. 1d; monkey 1: 3,825 peri-reach trials, 2,921 post-reach trials; monkey 2: 6,635 peri-reach trials, 4,329 post-reach trials).

Neurophysiological experiments

Experimental design. We performed neuronal recordings during a subset of task conditions used to study behaviour. In the RS task, the second target was either presented 10–300 ms after the reach completion, which we refer to as peri-reach trials, or 500–800 ms after reach completion, which we refer to as post-reach trials. In the SS task, the second target was presented 200–1,000 ms after the first saccade to temporally match the second target presentation to that in the RS task, accounting for the duration of the reach, which we refer to as saccade trials. On average, the reach was initiated 165 ± 39 ms (monkey 1, mean ± s.d., 124–218 interdecile range) or 123 ± 65 ms (monkey 2, mean ± s.d., 94–153 interdecile range) after the Go cue with a reach duration of 171 ± 42 ms (monkey 1, mean ± s.d., 128–211 interdecile range) or 122 ± 33 ms (monkey 2, mean ± s.d., 91–159 interdecile range). We defined the 350-ms time period before the onset of the second target as the gaze-anchoring epoch. On peri-reach trials, the gaze-anchoring epoch included activity related to reach execution, reach preparation and the coordinated saccade. On post-reach trials and saccade trials, these processes were weaker or absent during the gaze-anchoring epoch.

Neural recordings were made from area LIP and the PRR on the lateral and medial banks of the intraparietal sulcus using multiple-electrode microdrives (Double MT, Alpha Omega; Extended Data Fig. 2). Neurons were recorded within 5–8 mm of the cortical surface. Spiking and LFP activity were recorded with glass-coated tungsten electrodes (Alpha Omega) with impedance 0.7–1.4 MΩ measured at 1 kHz (Bak Electronics). Neural signals were amplified (×10,000; TDT Electronics), digitized at 20 kHz with 12 bits per sample (National Instruments), and continuously streamed to disk during the experiment (custom C and MATLAB 2019a code). Broadband neural activity was preprocessed to obtain single-unit spike times and LFP activity. All significant differences in firing rates for this study were determined using a random permutation test with 10,000 permutations.

During the experiment, we analysed the activity of each neuron from area LIP recorded in the centre-out saccade task to assess spatial selectivity. If the LIP neuron appeared to show spatial selectivity, the double-step tasks were run, including all of the test conditions described above. We placed the second target for the double-step tasks either within the response field for an area LIP neuron being recorded, or at an alternative location in the same visual hemi-field outside the response field. During the experiment, PRR neurons were isolated and recorded regardless of their response properties.

Area LIP neuronal database. Area LIP neurons were isolated and mapped for spatial selectivity using a visually guided, centre-out, delayed saccade to eight possible target locations, as described above. After the experiment, if the cell showed a significant increase in activity during the delay period of the centre-out task relative to the baseline period for a given target ($P < 0.05$, permutation test), the cell was determined to be spatially selective and that target was labelled as being in the preferred direction of the cell. Each LIP cell was recorded for a minimum of 10 trials in the preferred direction for each task condition (peri-reach, post-reach and saccade trials). If the LIP cell met these two criteria (spatial selectivity in a centre-out task and minimum number of trials), the cell was included in the database. There were no inclusion or exclusion criteria for the LIP neurons based on neural responses in either of the double-step tasks.

PRR neuronal database. After the experiment, we analysed the activity of each PRR neuron for responses to planning and executing the reach. In the database we only included PRR neurons that contained a significant response during the delay and reach execution periods of the RS task when compared to the baseline epoch of that task. For a minority of PRR neurons (13 of 34 neurons), we also confirmed that the location of the first movement was in the response field by mapping the response field in the centre-out reach-and-saccade task using 4–8 targets. PRR neurons that did not respond to the first movement of the RS task compared to the baseline and PRR neurons with responses to other target locations were excluded from further analysis. Consequently, the first movement of the RS task was in the reach response field of the PRR neurons under study.

Firing rate RS/SS task selectivity. We estimated peri-stimulus time histograms with a 20-ms smoothing window. We defined a task selectivity index that measured the mean fractional difference (MFD) in firing rate between the RS and SS task trials ((RS − SS)/SS) during the gaze-anchoring epoch. We tested for significant differences between the RS and SS task trials by comparing the measured task selectivity index with a null distribution of task selectivity indices when randomly permuting the RS and SS task labels on each trial. Results are presented in Fig. 1g.

Firing rate versus SSRT. We measured the association between the second saccade reaction time and the firing rate of area LIP and PRR neurons by performing linear regression and reporting the slope, statistical significance and correlation coefficient separately for peri-reach, post-reach and saccade trials. Results are presented in Fig. 1h.

LFP phase. We subtracted the mean LFP response from each trial to suppress the influence of responses evoked by the stimuli and responses. We then band-pass filtered the LFP at 20 Hz to study beta-frequency activity and at 40 Hz to study gamma-frequency activity. Band-pass filtering was performed with multitaper methods ($T = 200$ ms, $W = 5$ Hz (ref. [39])). Owing to variability in the timing of the coordinated reach and saccade and the temporal smoothing necessary to resolve band-limited LFP phase, the peri-reach interval, and not the post-reach interval, potentially includes reach execution, reach preparation and the coordinated saccade.

Dual-coherent LFP phase. For each trial, we measured the phase of LFP activity at the time of the spiking activity by calculating the spike times within the analysis window and computing the phase of band-pass-filtered LFP activity at these times. The mean phase was calculated for each trial by calculating the circular mean across all spikes within the analysis window. We refer to this value as the spike-triggered dual-coherent LFP phase. For spike–LFP–LFP sessions, we calculated the spike-triggered LFP phase for each spike–LFP pair (ϕ_{PRR} and ϕ_{LIP}) and then the circular distance between the two phases, which we refer to as the dual-coherent phase (ϕ_{Dual}):

$$\phi_{Dual} = \text{angle}\left(\frac{e^{i\phi_{PRR}}}{e^{i\phi_{LIP}}}\right) \quad (1)$$

The circular statistics toolbox in MATLAB (The Mathworks) was used to perform statistical tests[40]. Results are presented in Fig. 2 and Extended Data Figs. 3, 5–9.

Phase analysis also allowed us to analyse trial-by-trial variations between the neural responses and behavioural effects such as the reaction time for the second saccade and accuracy of the reach, described below.

LFP phase difference and SSRT. For each trial, we measured the effect of the LFP phase alone on SSRT. For each area, we calculated the circular mean of the phase of the LFP across the analysis window. We then calculated the circular distance between the two phases in each area using Eq. 1 above. Results are presented in Extended Data Fig. 6.

Dual-coherent LFP phase versus SSRT (parametric approach). We modelled the SSRT from peri-reach, post-reach and saccade trials using a von Mises fit in which SSRT varies across trials according to a gamma distribution $\Gamma(k,\theta)$ with constant scale, k, and a rate, θ, that depends on the phase, ϕ, on that trial during the last 350 ms preceding the onset of the second target according to a von Mises function, $\theta = A + B\ \exp(\kappa\ \cos(\phi - \mu))$. We defined three different versions of the model each containing the same number of parameters in which phase was set by the PRR-only phase, the LIP-only phase or the dual-coherent phase. The gamma-scale parameter, k, and the von Mises fit parameters, A, B, κ, μ, were estimated using maximum likelihood. The null hypothesis was that SSRT varied across trials according to a gamma distribution with constant scale and rate parameters and did not vary with phase. For each version of the model, the likelihood was maximized using the function mle in MATLAB (MATLAB 2019a, Mathworks). We fitted parameters using a two-step procedure. In step 1, we initialized parameters based on heuristics derived from the SSRT versus phase tuning curve. The offset, A, was initialized at the minimum of the tuning curve. The magnitude, B, was initialized using the range of the tuning curve. The preferred phase, μ, was initialized at the phase with the maximum of the tuning curve. The dispersion, κ, was initialized at 0.5 based on visual inspection of the tuning curves. The scale, k, was also initialized at 20 based on visual inspection of the SSRT distributions. When tuning was weaker, the fits based on initializing founded on heuristics became trapped in local minima. In such cases, we pursued step 2. In step 2, we generated surrogate datasets by jittering the SSRT observations by adding a random value less than 1% of the original data and refitting the data using the same heuristics as before. We then used the parameter fits obtained from the surrogate data to initialize the optimization for the original data and repeated the optimization based on these initial conditions. We tested the significance of the von Mises fit for each version of the model against the null hypothesis using a likelihood-ratio test. We selected between the models based on the dual-coherent phase, the LIP-only phase and the PRR-only phase according to the difference in the maximized log likelihood according to Akaike information criterion (AIC). For each model, we also estimated and compared the generalization error using k-fold cross-validation with 10 folds. Results are presented in Fig. 2d and Extended Data Fig. 4a, b.

To test the dependence of the dual-coherent phase on spike timing, we repeated the analysis described above after jittering the spike times on each trial according to a Gaussian distribution with standard deviation of 2 ms, 5 ms,10 ms or 20 ms. Results are presented in Extended Data Fig. 8.

Dual-coherent LFP phase versus reach accuracy (parametric approach). We modelled the accuracy of the reach on peri-reach and post-reach trials according to a von Mises fit in which reach error varies across trials according to a gamma distribution $\Gamma(k, \theta)$ with constant scale, k, and a rate, θ, that depends on the phase, ϕ, on that trial during the last 350 ms preceding the onset of the second target according to a von Mises function, $\theta = A + B\ \exp(\kappa\ \cos(\phi - \mu))$. We defined three different versions of the model, each containing the same number of parameters in which the phase was set by the PRR-only phase, the LIP-only phase or the dual-coherent phase. For each model, the gamma-scale parameter, k, and the von Mises fit parameters, A, B, κ, μ, were estimated using maximum likelihood. The null hypothesis was that reach error varied across trials according to a gamma distribution with constant scale and rate parameters and did not vary with phase. The likelihood was maximized using the function mle in MATLAB 2019a (Mathworks) using the same two-step procedure as detailed above for SSRT. We tested the significance of the von Mises fit for each version of the model against the null hypothesis using a likelihood-ratio test. We selected between the models based on the dual-coherent phase, the LIP-only phase and the PRR-only phase according to the difference in the maximized log likelihood according to AIC. For each model, we also estimated the generalization error using k-fold cross-validation with 10 folds. Results are presented in Fig. 2f, Extended Data Fig. 4c, d.

Reach accuracy and SSRT versus phase (non-parametric approach). We performed a non-parametric test of the effects of phase on behavioural performance, reach error and SSRT. For each metric, we computed the resultant vector using eight equally spaced and sized phase bins. To determine significance, we performed a permutation test by permuting the phase on each trial and recalculating the resultant vector (10,000 permutations).

Two-sample non-parametric phase tuning. We used a non-parametric test of the effects of phase on behavioural performance to compare resultant vectors across different phase measurements (for example, beta-LFP versus gamma-LFP dual coherence). We performed the permutation test by calculating the difference in resultant vectors and comparing to the resultant when permuting the phases across populations (10,000 permutations). Results are presented in Extended Data Figs. 8, 9.

Reach-start aligned analysis. We analysed the relationship between LFP phase, SSRT and reach error during a 350-ms time epoch aligned to the start of the reach. The reach-start analysis window extends from 200 ms before the start of the reach until 150 ms after the start of the reach. As the reach duration was typically 100–200 ms (see Extended Data Fig. 1), the reach-start analysis window spans the reach execution period. This interval was chosen to be close in time to the gaze-anchoring window while avoiding confounding influences due to presentation of the Go cue and the second saccade target. Earlier time intervals included the onset of the Go cue, whereas later time intervals included the onset of the second saccade target. Results are presented in Extended Data Fig. 5.

Dual-coherent LFP phase, firing rate and SSRT. We measured the association between the SSRT and the firing rate of PRR neurons for trials grouped by spike-triggered phase by performing linear regression. We report the statistical significance of the preferred and null phase bins. Results are presented in Fig. 3a–c.

Dual-coherent LFP phase versus firing rate. We modelled the firing rate on peri-reach, post-reach and saccade trials according to a von Mises fit in which spike count varies across trials according to a Poisson distribution with rate, λ, that depends on the phase, ϕ, on that trial during the last 350 ms preceding the onset of the second target according to a von Mises function, $\lambda = A + B\ \exp(\kappa\ \cos(\phi - \mu))$. The von Mises fit parameters, A, B, κ, μ, were estimated using maximum likelihood. The null hypothesis was that spike count across trials varied according to a Poisson distribution with constant rate parameter. The likelihood for each model was maximized using the function mle in MATLAB (Mathworks). We tested for significance of the von Mises fit against the null hypothesis using a likelihood-ratio test. Results are presented in Fig. 4c, d and Extended Data Fig. 10.

Inhibitory channel modulation model. We modelled the firing rate of LIP neurons (Rate_{LIP}) trial-by-trial as a function of the LIP base firing rate on that trial, (Base_{LIP}), the PRR spike rate on that trial (Rate_{PRR})and the dual-coherent beta-LFP phase on that trial (ϕ_{Dual}) according to an inhibitory channel modulation model. The model operates according

to two functions (see Fig. 4a): inhibitory input gain function models the inhibitory gain (I_t) based on the PRR firing on that trial, and a modulation state function models the modulation state (M_t) based on the dual-coherent beta-LFP phase on that trial:

$$\text{Rate}_{\text{LIP}} = \text{Base}_{\text{LIP}} - (I_t \times M_t) \quad (2)$$

The inhibitory input gain function and modulation state function were fit by binning trials based on the PRR spike rate and fitting a von Mises function to the SSRTs in each bin according to the dual-coherent phase (see Fig. 3a). Trials were grouped in increments of 8 spikes per second. The inhibition scale factor for each firing rate bin was measured as the weighted difference between the peak of the von Mises function fit to that bin and the mean SSRT across all peri-reach trials (see Fig. 3d). The inhibitory gain on each trial (I_t) was defined according to an exponential function consisting of two parameters (α, β) and the PRR firing rate on that trial (Rate_{PRR}):

$$I_t = \alpha \exp(\beta \, \text{Rate}_{\text{PRR}}) - \alpha \quad (3)$$

The parameters of the inhibitory input gain function (α, β) were fit using the scale factors of the von Mises fit to each firing rate bin (see Fig. 3e). The modulation state for each trial was defined according to a von Mises distribution with two parameters (κ, μ) and the dual-coherent beta-LFP phase on that trial (ϕ_{Dual}):

$$M_t = \exp(\kappa \cos(\phi_{\text{Dual}} - \mu)) \quad (4)$$

The parameters of the modulation state function (κ, μ) were calculated from the average of the von Mises parameters fit across bins of PRR firing rates and SSRTs ($\kappa = 1.5, \mu = 65$; see Fig. 3d). We describe the goodness of fit (R^2) using the adjusted R^2 value, which is the ratio of the sum of the squared error to the sum of the squared total, scaled to account for the number of observations and the number of predictors.

LIP spike rates were not used in fitting either the inhibitory gain function or the modulation state function. The inhibitory channel model only depends on the LIP spiking activity for a base rate starting point for the model on each trial. The LIP base rate (Base_{LIP}) on each trial (t) was defined by the average LIP firing rate recorded before suppression of the firing rate is observed (MeanPreMove) and the difference between the LIP firing rate before movement onset (preMove(t)) and before the onset of the second target (preTarg(t)) on each trial such that:

$$\text{Base}_{\text{LIP}}(t) = \text{MeanPreMove} + (\text{preMove}(t) - \text{preTarg}(t)) \quad (5)$$

We characterized the performance of the model by calculating the mean squared error (MSE) between the observed LIP firing rate on each trial and the predicted LIP firing rate on each trial according to the model. For comparison, we also calculated the MSE for an input gain function-only model, which did not include the modulation state function, a modulation state-only model, which did not include the inhibitory input gain function, and a linear regression model. The linear regression, unlike the other models, was fit using the observed LIP firing rates on each trial.

Reporting summary

Further information on research design is available in the Nature Research Reporting Summary linked to this paper.

Data availability

Data for the current study are available on a GitHub repository: https://bitbucket.org/pesaranlab/doublestep/.

Code availability

The MATLAB code for current study is available on a GitHub repository: https://bitbucket.org/pesaranlab/doublestep/.

39. Mitra, P. P. & Pesaran, B. Analysis of dynamic brain imaging data. *Biophys. J.* **76**, 691–708 (1999).
40. Berens, P. CircStat: a MATLAB toolbox for circular statistics. *J. Stat. Softw.* **31**, 1–21 (2009).

Acknowledgements We thank R. Comeau, S. Frey and B. Hynes for custom modifications to the BrainSight system, and N. Price, E. Zavitz, A. Charles and members of the Pesaran laboratory for helpful feedback. This work was supported, in part, by NIH T32 EY007136 (M.A.H.), ARC DE180100344 (M.A.H.), NHMRC APP1185442 (M.A.H.), NSF CAREER Award BCS-0955701 (B.P.), NEI R01-EY024067 (B.P.), the Army Research Office (B.P.), the Simons Foundation (B.P.), McKnight Scholar Award (B.P.), Sloan Research Fellowship (B.P.) and NIH R01-NS104923 (B.P.).

Author contributions M.A.H. and B.P. conceptualized the project and designed the experiments. M.A.H. performed the experiments. M.A.H. and B.P. analysed the data and wrote the manuscript.

Competing interests The authors declare no competing interests.

Additional information

Supplementary information The online version contains supplementary material available at https://doi.org/10.1038/s41586-022-04631-2.

Correspondence and requests for materials should be addressed to Bijan Pesaran.

Peer review information *Nature* thanks Martin Giese, Nicholas Hatsopoulos and Lawrence Snyder for their contribution to the peer review of this work. Peer reviewer reports are available.

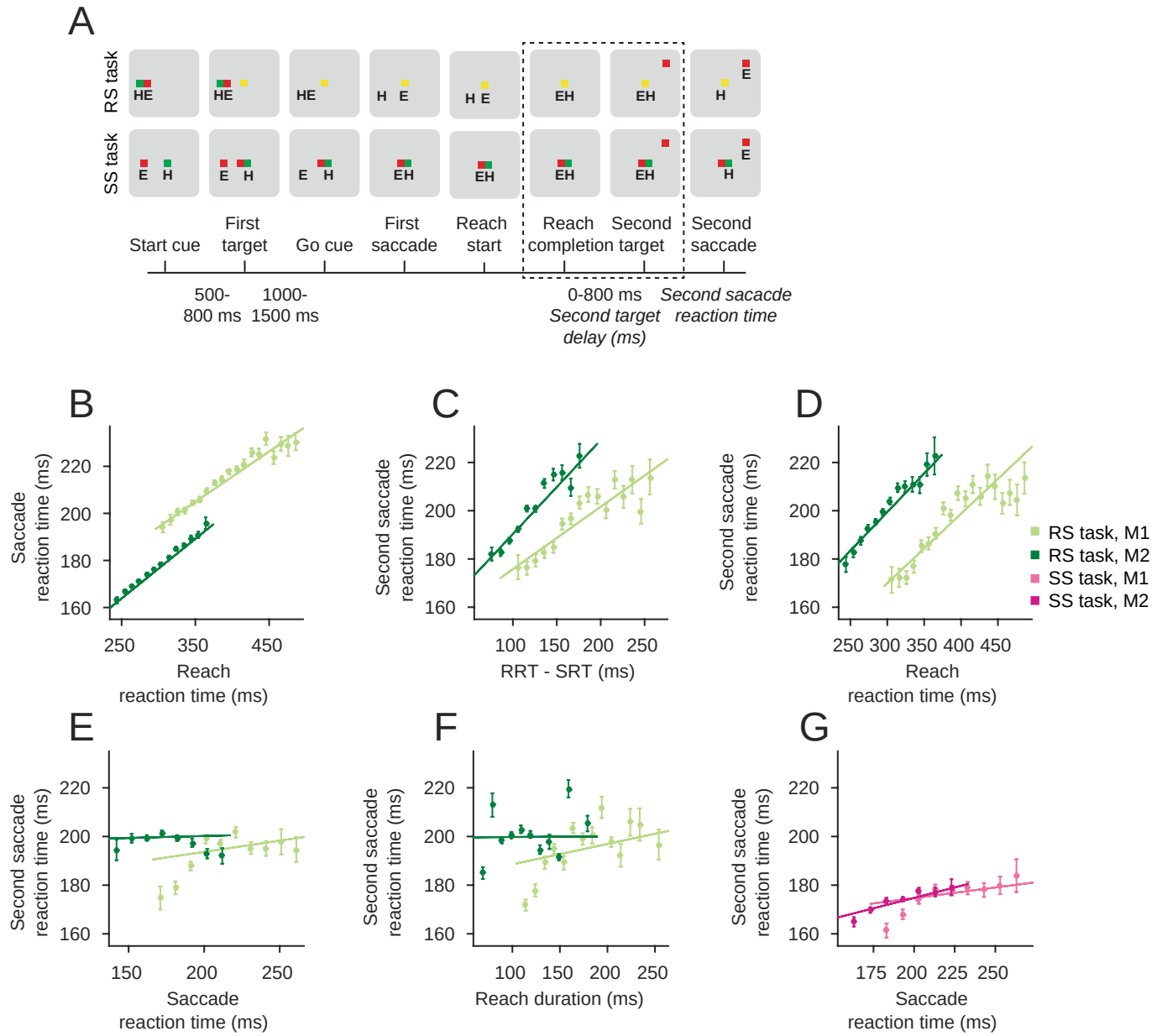

Extended Data Fig. 1 | Coordinated and independent movement tasks. **a**, Reach and saccade double-step task (RS) and Saccade double-step task (SS), indicating hand (H) and eye (E) position at each epoch. Dashed lines indicate period of gaze-anchoring in the RS task, and temporally matched epochs in the SS task. The slowing of the second saccade reaction time (SSRT) was tied to the coordinated movement. **b**, The coordination of the first movement was established by the strong correlation between the reaction times for the reach and saccade in the first movement (Monkey 1 (M1): R = 0.34, slope = 0.21 ms/ms, $p = 3 \times 10^{-139}$, Monkey 2 (M2): R = 0.45, slope = 0.25 ms/ms, p = 0, Pearson pairwise linear correlation). **c**, SSRT correlated with the difference between the reaction times of the reach and saccade in the first movement (M1: R = 0.20, slope = 0.26 ms/ms, $p = 2 \times 10^{-49}$, M2: R = 0.22, slope = 0.39 ms/ms, $p = 2 \times 10^{-78}$, Pearson pairwise linear correlation). **d**, Specifically, SSRT correlated with the reaction time of the reach (M1: R = 0.23, slope = 0.29 ms/ms, $p = 4 \times 10^{-63}$, M2: R = 0.20, slope = 0.32 ms/ms, $p = 2 \times 10^{-65}$, Pearson pairwise linear correlation). **e**, The SSRT was not dependent on the reaction time of the saccade in the RS task (M1: R = 0.05, slope = 0.09 ms/ms, $p = 8 \times 10^{-4}$, M2: R = 0.006, slope = 0.02 ms/ms, p = 0.63, Pearson pairwise linear correlation). **f**, SSRT did not depend on the duration of the reach (M1: R = 0.07, slope = 0.08 ms/ms, $p = 1 \times 10^{-6}$, M2: R = 0.001, slope = 0.002 ms/ms, p = 0.91, Pearson pairwise linear correlation). **g**, SSRT only weakly correlated with the SRT in the SS task (M1: R = 0.06, slope = 0.08 ms/ms, $p = 1 \times 10^{-3}$, M2: R = 0.12, slope = 0.17 ms/ms, $p = 7 \times 10^{-13}$, Pearson pairwise linear correlation). Therefore, the slowing of the SSRT was tied to coordinated movement, and primarily the timing of the reach. Monkey 1: RS task, n = 10,324 trials, SS task, n = 8,372 trials; Monkey 2: RS task, n = 12,840 trials, SS task n = 8,452 trials. All error bars show mean ± SEM.

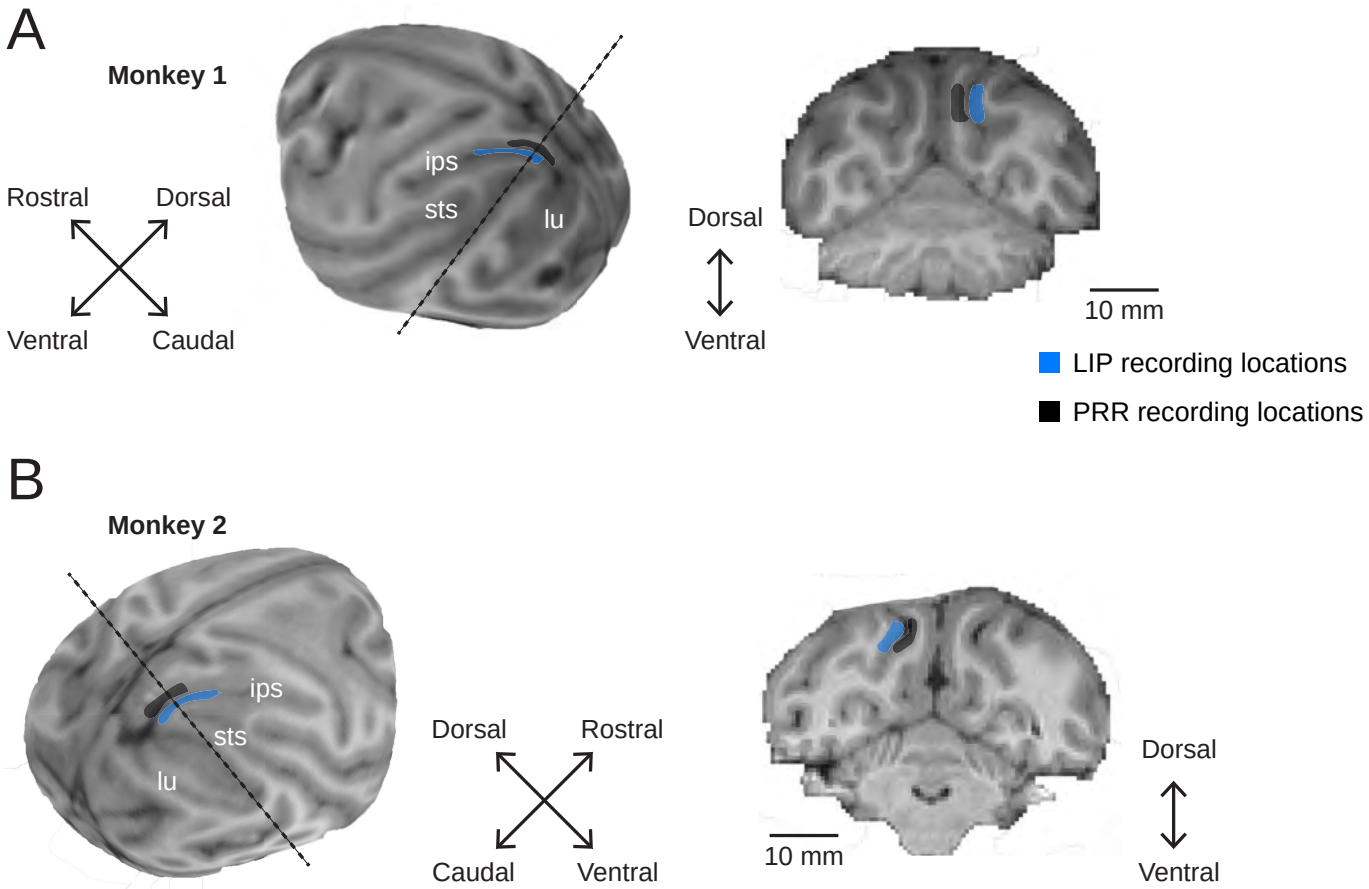

Extended Data Fig. 2 | Anatomical locations of recordings. Recording chambers were placed over the posterior parietal cortex of the hemisphere contralateral to the reaching arm. **a**, **b**, Whole brain MRI reconstructions and example coronal slice from Monkey 1 (**a**) and Monkey 2 (**b**). Chamber placement and electrode recording sites were registered to the structural MRI (BrainSight, Rogue Research). Recording regions for area LIP (blue) and PRR (black) are indicated by the shaded regions. Dashed lines indicate the plane of example coronal sections shown. Key sulcal landmarks, intraparietal sulcus (ips), lunate sulcus (lu) and superior temporal sulcus (sts), are also indicated.

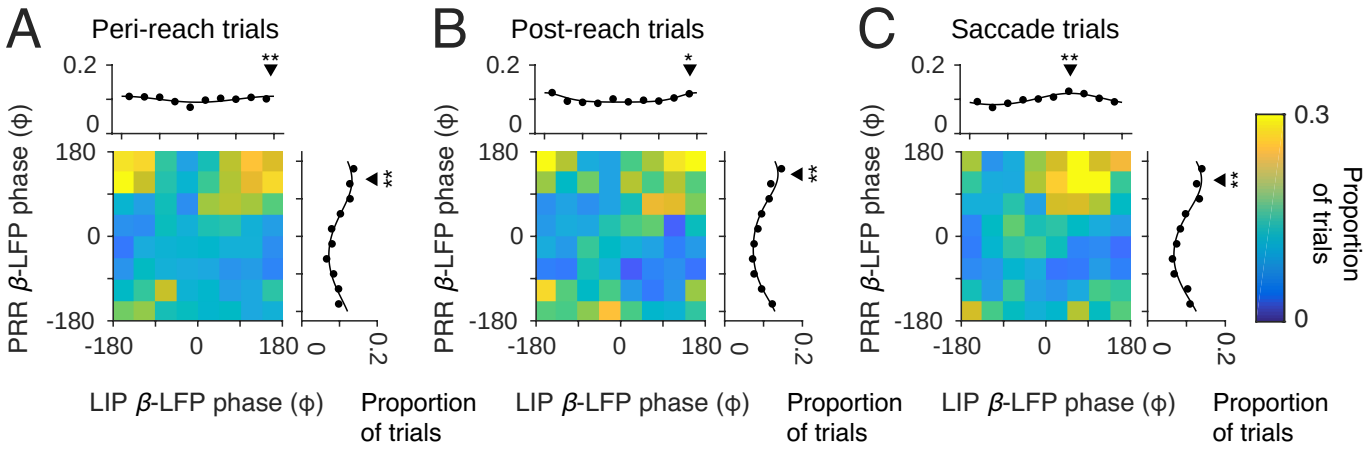

Extended Data Fig. 3 | Phase of spike-β-LFP coherence in each cortical area. **a**–**c**, Peri-reach (**a**), post-reach (**b**), and saccade (**c**) trials showing spike-LFP coherence between PRR spiking and PRR LFP phase (y-axis) and LIP LFP phase (x-axis) in the beta-band (β, 20 Hz, colorscale: proportion of trials). Marginals show the proportion of trials as a function of phase in each area. **Peri-reach:** PRR β-LFP $p = 2 \times 10^{-49}$, mean phase = 136 ± 75°; LIP β-LFP $p = 8 \times 10^{-5}$, mean phase = 172 ± 79°, **Post-reach:** PRR β-LFP $p = 4 \times 10^{-57}$, mean phase = 149 ± 74°, LIP β-LFP p = 0.02, mean phase = 164 ± 79°, **Saccade trials:** PRR β-LFP $p = 2 \times 10^{-52}$, mean phase = 135 ± 73°, LIP β-LFP $p = 2 \times 10^{-52}$, mean phase = 59 ± 78°, Rayleigh's test of non-uniformity, circular mean ± SD phase). Black triangles indicate mean phase, stars indicate that the distribution is non-uniform (one star, $p < 0.05$; two stars, $p < 0.01$, exact p-values above). Peri-reach: n = 4814 trials, Post-reach: n = 2116 trials, Saccade: n = 3583 trials (same dataset shown in Figs. 2, 3). All error bars show mean ± SEM.

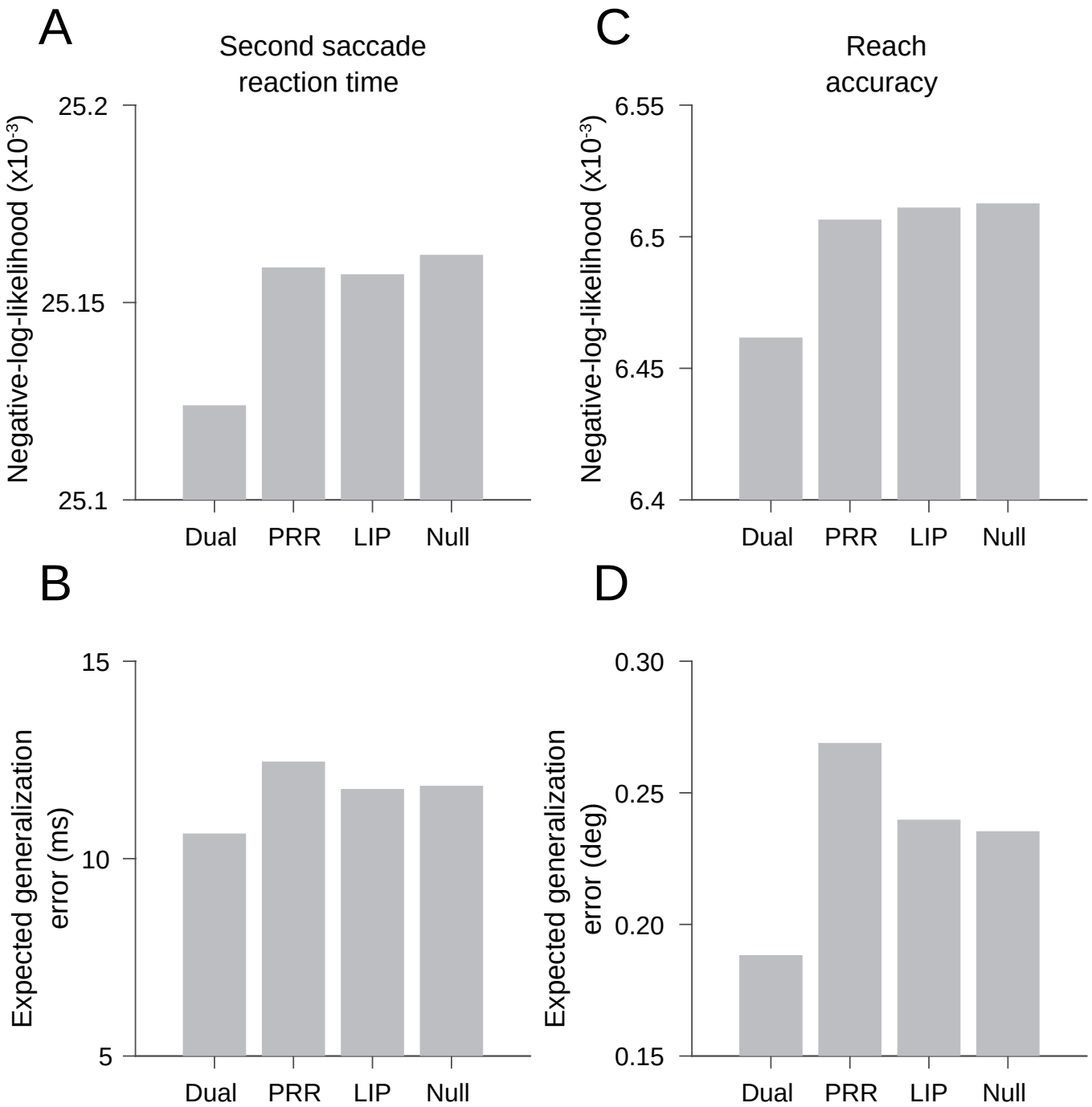

Extended Data Fig. 4 | Negative-log-likelihood and generalization errors for model fits. Second saccade reaction time: a, Dual-phase negative-log-likelihood (NLL) = 25124; PRR-only phase NLL = 25158; LIP-only phase NLL = 25157; Null NLL = 25162; $\Delta NLL_{Dual\text{-}PRR} = 35$; $\Delta NLL_{Dual\text{-}LIP} = 33$, AIC test. **b**, Expected generalization error: Dual-coherent: 10.6 ms, R = 0.10; PRR-only: 12.5 ms, R = −0.05; LIP-only: 11.8 ms, R = 0.01; Null: 11.8 ms, where R = 1-(SSE_model/SSE_null). **Reach accuracy: c**, Dual-phase negative-log-likelihood (NLL)= 6462; PRR-only phase NLL = 6507; LIP-only phase NLL = 6511; Null NLL = 6512; $\Delta NLL_{Dual\text{-}PRR} = 45$; $\Delta NLL_{Dual\text{-}LIP} = 49$, AIC test. **d**, Expected generalization error: Dual-coherent: 0.18 deg, R = 0.20, PRR-only: 0.27 deg, R = −0.14, LIP-only: 0.24 deg, R = −0.02, Null: 0.24 deg). Non-parametric analyses: Peri-reach trials: SSRT: dual-coherent: resultant = 6.2×10^{-3}, $p < 10^{-6}$, LIP-only: p = 0.28, PRR-only: resultant = 2.3×10^{-6}, p = 0.02, RA: dual-coherent: resultant = 1.6×10^{-4}, p = 0. LIP-only: p = 0.33. PRR-only: resultant = 5.3×10^{-5}, $p = 1.6 \times 10^{-3}$. Post-reach trials for dual coherent phase: SSRT: resultant = 5.7×10^{-3}, p = 0. post-reach RA: resultant = 2.1×10^{-4}, $p = 1.2 \times 10^{-3}$. Saccade trials: SSRT: p = 0.89. Peri-reach: n = 4814 trials, Post-reach: n = 2116 trials, Saccade: n = 3583 trials (same dataset shown in Figs. 2, 3).

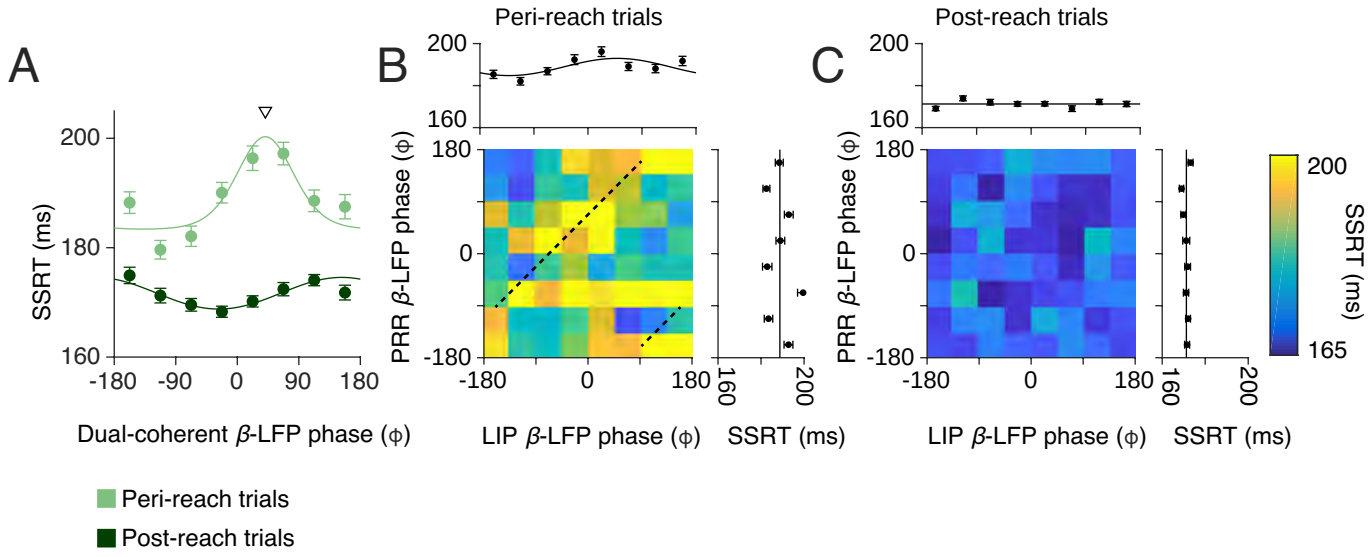

Extended Data Fig. 5 | Dual coherent β-LFP phase aligned to reach onset. **a**, Second saccade reaction time (SSRT) against dual-coherent β-LFP phase for each RS task trial type (Peri-reach: light green. Post-reach: dark green) during the gaze anchoring epoch when aligned to reach onset, instead of second target onset. Solid lines present changes in SSRT fitted by von Mises function (peri-reach: $p = 0$, preferred phase = 41°. post-reach: $p = 6 \times 10^{-5}$, preferred phase = 153°). Downward triangle presents the mean of the von-Mises fit dual-coherent β-LFP phase at maximum SSRT on peri-reach trials. **b**, **c**, Phase of spike-β-LFP coherence in each cortical area (PRR β-LFP coherence, y axis; LIP β-LFP coherence, x axis) and influence on SSRT (colorscale). Marginals show SSRT against β-LFP phase coherence in each area alone (Peri-reach: PRR-only $p = 0.53$, LIP-only $p = 2 \times 10^{-3}$, preferred phase = 48°. Post-reach: PRR-only $p = 0.53$, LIP-only $p = 0.48$) . Dashed lines (**b**) indicate the corresponding dual-coherent phase shown by the downward triangle in (**a**). Note that confounds due to the onset of the Go cue were not a concern because the LFP phase calculation during gaze-anchoring epoch rarely overlapped cue delivery (3.7% of peri-reach trials, 0% of post-reach trials and 2.5% of saccade trials). All p-values report likelihood-ratio test. Peri-reach: n = 4814 trials, Post-reach: n = 2116 trials, Saccade: n = 3583 trials (same dataset shown in Figs. 2, 3). All error bars show mean ± SEM.

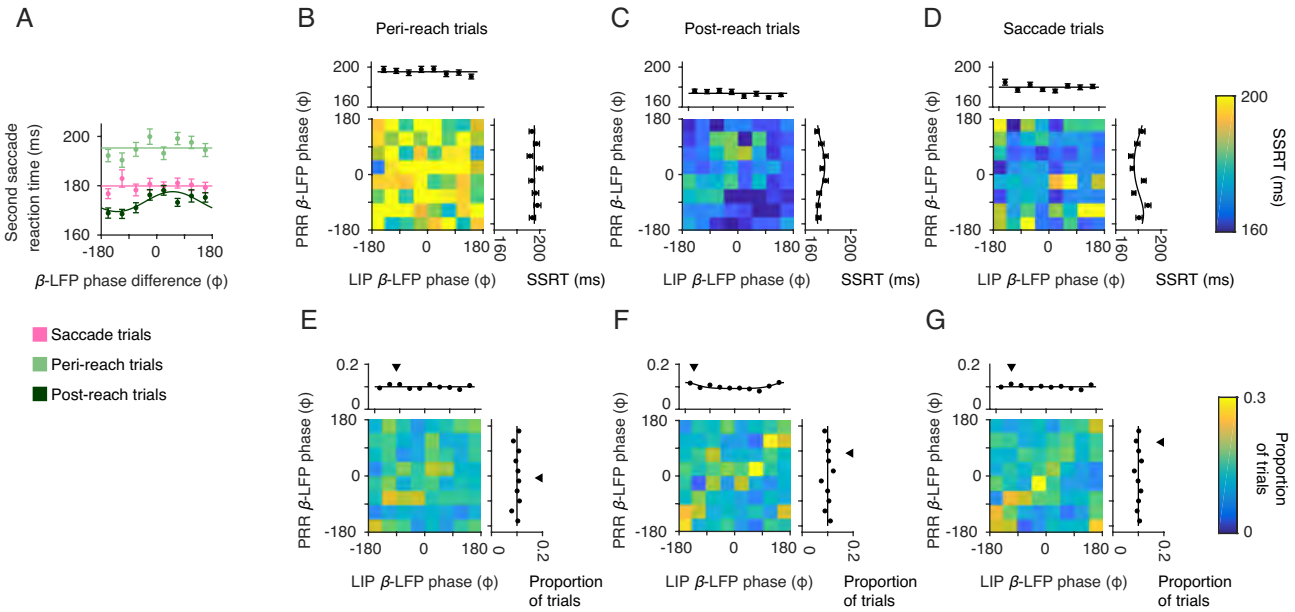

Extended Data Fig. 6 | *β*-LFP phase difference alone did not predict gaze anchoring. The circular mean *β*-LFP phase was taken across the gaze-anchoring epoch, irrespective of spike timing. **a**, Mean phase difference of the *β*-LFP (20 Hz) across cortical areas for each task trial type (Saccade: pink. Peri-reach: light green. Post-reach: dark green). Solid lines present changes in SSRT fitted by von Mises function (Peri-reach: p = 0.23. Post-reach: $p = 1 \times 10^{-3}$, preferred phase = 53°. Saccade: p = 0.83. likelihood-ratio test). **b**–**d**, Mean *β*-LFP phase in each cortical area (PRR *β*-LFP phase, y axis; LIP *β*-LFP phase x axis) and influence on SSRT (colorscale). Marginals show SSRT as a function of mean *β*-LFP phase in each area alone (Peri-reach: PRR-only p = 0.89, LIP-only p = 0.24. Post-reach: PRR-only $p = 8 \times 10^{-3}$, preferred phase = 32° LIP-only p = 0.20. Saccade: PRR-only $p = 8 \times 10^{-4}$, preferred phase = −143; LIP-only p = 0.12. likelihood-ratio test). **e**–**g**, *β*-LFP phase in PRR (y-axis) and LIP (x-axis, colorscale: proportion of trials). Downward triangles show the circular mean phase. Peri-reach: n = 4814 trials, Post-reach: n = 2116 trials, Saccade: n = 3583 trials (same dataset shown in Figs. 2, 3). All error bars show mean ± SEM.

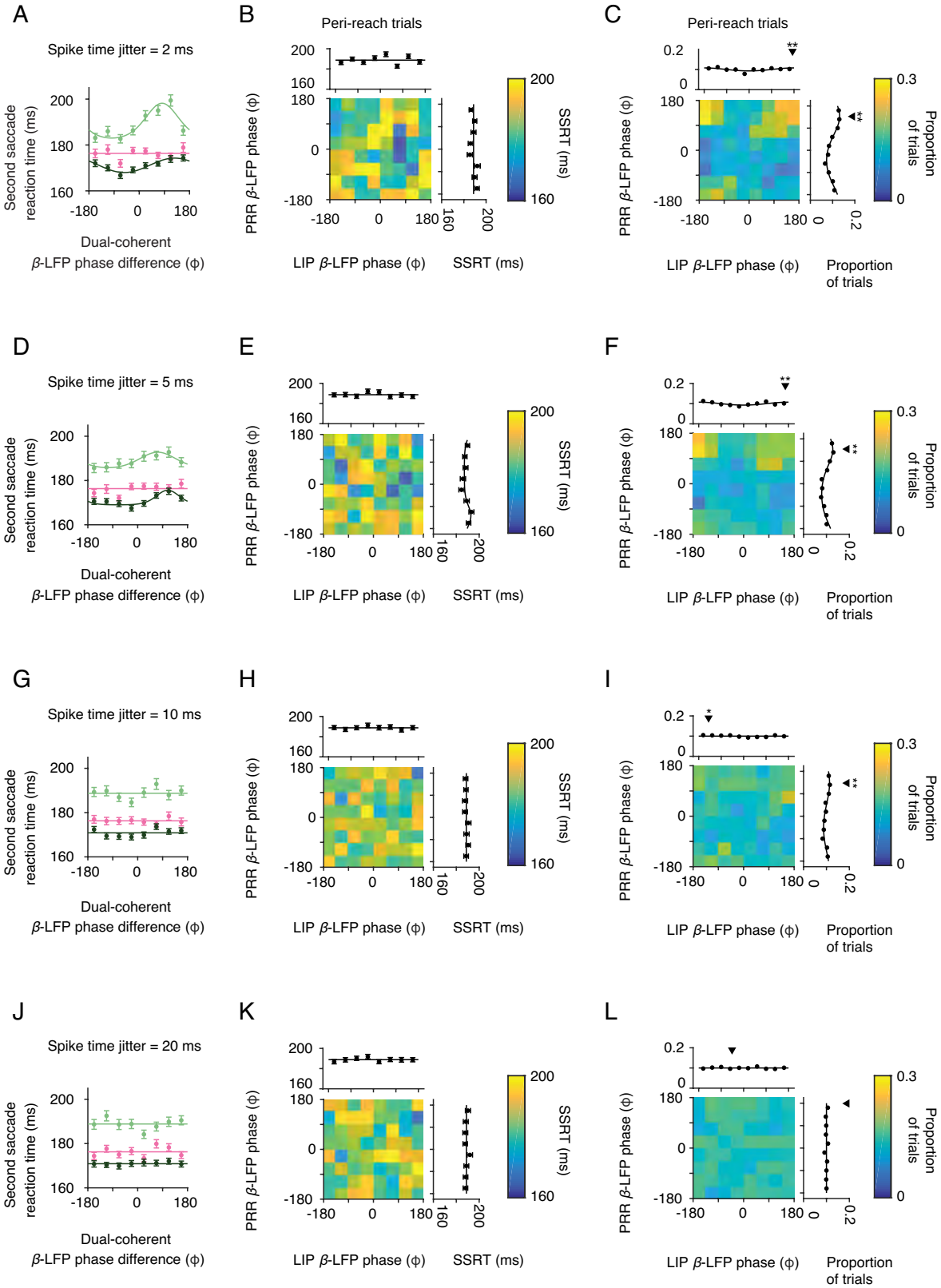

Extended Data Fig. 7 | See next page for caption.

Extended Data Fig. 7 | Spike timing dependence of dual coherent β-LFP phase. a–**l**, For each trial, spike times were jittered according to a Gaussian distribution with standard deviation 2 ms (**a**–**c**), 5 ms (**d**–**f**), 10 ms (**g**–**i**) and 20 ms (**j**–**l**). Second saccade reaction time (SSRT) as a function of dual-coherent β-LFP phase for each task trial type (Saccade, pink; Peri-reach, light green; Post-reach, dark green) during the gaze anchoring epoch was recomputed with the jittered spike times. Solid lines present changes in SSRT fitted by von Mises function (**a**, Peri-reach: $p = 1 \times 10^{-13}$, preferred phase = 82°. Post-reach: $p = 5 \times 10^{-5}$, preferred phase = 126°. Saccade: p = 0.68. **d**, Peri-reach: $p = 3 \times 10^{-3}$, preferred phase = 73°. Post-reach: $p = 7 \times 10^{-5}$, preferred phase = 108°. Saccade: p = 0.23. **g**, Peri-reach: p = 0.22. Post-reach: p = 0.29. Saccade: p = 0.90. **j**, Peri-reach: p = 0.11. Post-reach: p = 1. Saccade: p = 0.38. likelihood-ratio test). For peri-reach trials, the phase of spike-β-LFP coherence in each cortical area were computed for the jittered spike times (PRR β-LFP coherence, y axis; LIP β-LFP coherence x axis) and influence on SSRT (colorscale). Marginals show SSRT as a function of β-LFP phase coherence in each area alone (**b**, PRR-only p = 0.10, LIP-only, p = 0.10, **e**, PRR-only p = 0.04, preferred phase = −127°, LIP-only, p = 0.47, **h**, PRR-only p = 0.68, LIP-only, p = 0.63, **k**, PRR-only p = 0.52, LIP-only, p = 0.71, likelihood-ratio test). Spike-LFP coherence between PRR spiking and each cortical area alone for jittered spike times on peri-reach trials (PRR LFP phase, y-axis, LIP LFP phase x-axis, colorscale: proportion of trials). Marginals show the proportion of trials as a function of phase in each area (**c**, PRR $p = 2 \times 10^{-47}$, mean = 137°, LIP $p = 8 \times 10^{-4}$, mean = 175°, **f**, PRR $p = 2 \times 10^{-31}$, mean = 139°, LIP $p = 1 \times 10^{-3}$, mean = 167°, **i**, PRR $p = 3 \times 10^{-10}$, mean = 132°, LIP p = 0.04, mean = −140°, **l**, PRR p = 0.84, LIP p = 0.79, Rayleigh's test of non-uniformity, circular mean phase). Black triangles indicate mean phase, stars indicate that the distribution is non-uniform (one star, $p < 0.05$; two stars, $p < 0.01$, exact p-values above). Peri-reach: n = 4814 trials, Post-reach: n = 2116 trials, Saccade: n = 3583 trials (same dataset shown in Figs. 2, 3). All error bars show mean ± SEM.

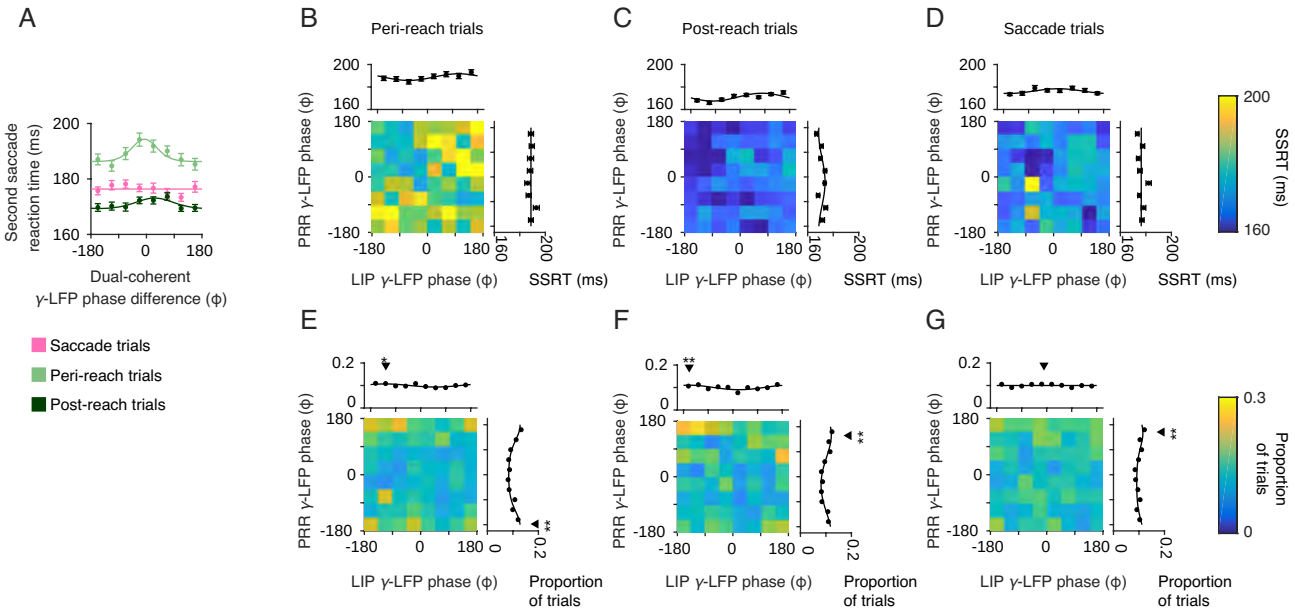

Extended Data Fig. 8 | Dual coherent γ-LFP phase. Dual-coherent phase was calculated between PRR spiking and the γ-LFP phase (40 Hz) in each cortical area. **a**, Second saccade reaction time (SSRT) against dual-coherent γ-LFP phase for each RS task trial type (Peri-reach = light green; Post-reach = dark green). Solid lines present changes in SSRT fitted by von Mises function (Peri-reach: $p = 8 \times 10^{-4}$, preferred phase = −6°. Post-reach: p = 0.04, preferred phase = 26°. Saccade: p = 0.1likelihood-ratio test). **b**–**d**, Mean γ-LFP phase in each cortical area (PRR γ-LFP phase, y axis; LIP γ-LFP phase x axis) and their influence on SSRT (colorscale). Marginals show SSRT against mean γ-LFP phase in each area alone (Peri-reach: PRR-only p = 0.55, LIP-only p = 0.02, preferred phase = 112°. Post-reach: PRR-only p = 0.02, preferred phase = −25°. LIP-only $p = 4 \times 10^{-6}$, preferred phase = 78°. Saccade: PRR-only p = 0.13, LIP-only p = 0.04, preferred phase = 17°, likelihood-ratio test). **e**–**g**, γ-LFP phase in PRR (y-axis) and LIP (x-axis, colorscale: proportion of trials). Marginals show the proportion of trials against phase in each area (Peri-reach: PRR $p = 4 \times 10^{-23}$, mean = −177°, LIP p = 0.02, mean = −125°. Post-reach: PRR $p = 2 \times 10^{-6}$, mean = 148°, LIP $p = 3 \times 10^{-4}$, mean = −159°. Saccade: PRR $p = 1 \times 10^{-4}$, mean = 153°, LIP p = 0.33, Rayleigh's test of non-uniformity). Black triangles indicate mean phase, stars indicate that the distribution is non-uniform (one star, $p < 0.05$; two stars, $p < 0.01$, exact p-values above). Peri-reach SSRT slowing with gamma-frequency phase was significantly reduced compared to that with beta-frequency dual-coherent phase (resultant = 2.9×10^{-3}, $p = 1 \times 10^{-4}$. permutation test). Peri-reach: n = 4814 trials, Post-reach: n = 2116 trials, Saccade: n = 3583 trials (same dataset shown in Figs. 2, 3). All error bars show mean ± SEM.

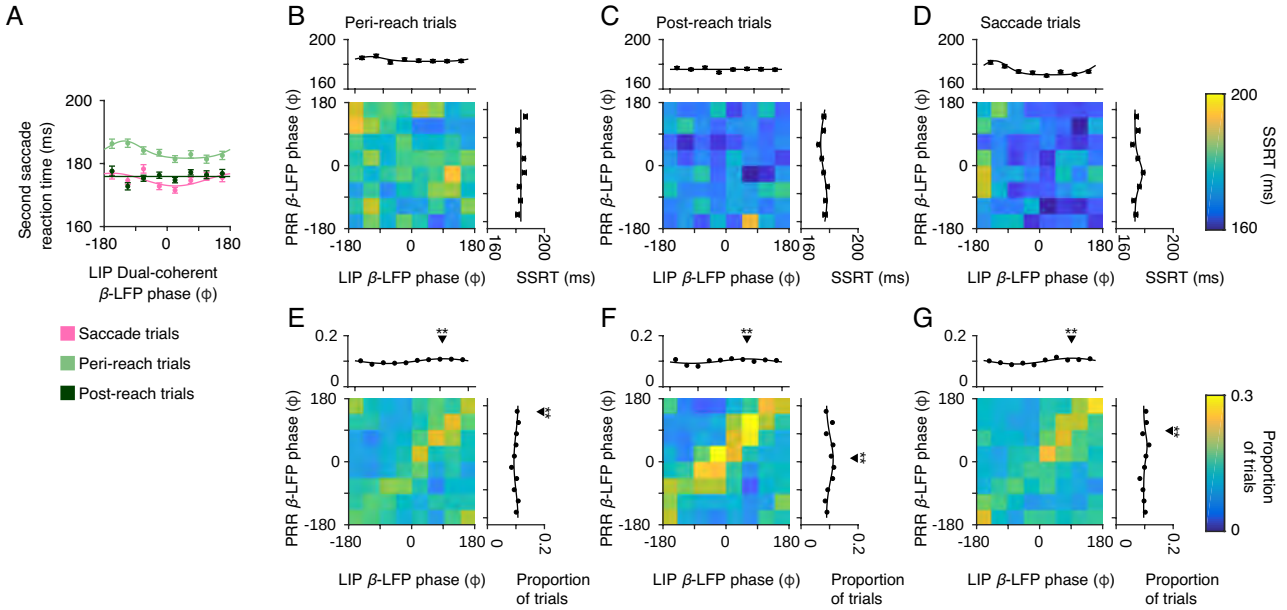

Extended Data Fig. 9 | LIP-spike dual coherent β-LFP phase. Dual-coherent phase was calculated between LIP spiking and the β-LFP phase (20 Hz) in each cortical area. **a**, Second saccade reaction time (SSRT) as a function of LIP dual-coherent β-LFP phase for each RS task trial type (peri-reach trials, light green; post-reach trials, dark green) and SS task trials (saccade trials). Solid lines present changes in SSRT fitted by von Mises function (peri-reach: $p = 1 \times 10^{-4}$, preferred phase = −122°. post-reach: $p = 0.21$. saccade: $p = 1 \times 10^{-3}$, preferred phase = −157°. likelihood-ratio test). SSRT varied with PRR-spike dual-coherent phase significantly more than with LIP-spike dual-coherent phase (resultant = 1.2×10^{-3}, $p < 10^{-6}$, permutation test). **b**–**d**, Mean LIP-spike β-LFP phase in each cortical area (PRR β-LFP phase, y axis; LIP β-LFP phase x axis) and their influence on SSRT (colorscale). Marginals show SSRT as a function of mean LIP-spike β-LFP phase in each area alone (Peri-reach: PRR-only $p = 0.23$. LIP-only $p = 0.49$. Post-reach: PRR-only $p = 6 \times 10^{-4}$, preferred phase = 109°. LIP-only $p = 0.48$. Saccade: PRR-only $p = 5 \times 10^{-5}$ preferred phase = −25°. LIP-only $p = 0$, preferred phase = −142°, likelihood-ratio test). **e**–**g**, LIP-spike β-LFP phase in PRR (y-axis) and LIP (x-axis, colorscale: proportion of trials). Marginals show the proportion of trials as a function of phase in each area (Peri-reach: PRR: $p = 2 \times 10^{-5}$, mean = 160°, LIP: $p = 1 \times 10^{-7}$, mean = 97°. Post-reach: PRR $p = 2 \times 10^{-5}$, mean = 11°, LIP $p = 5 \times 10^{-4}$, mean = 67°. Saccade: PRR $p = 2 \times 10^{-5}$, mean = 100°, LIP $p = 4 \times 10^{-12}$, mean = 103°, Rayleigh's test of non-uniformity, circular mean). Black triangles indicate mean phase, stars indicate that the distribution is non-uniform (one star, $p < 0.05$; two stars, $p < 0.01$, exact p-values above). Peri-reach: n = 7782 trials, Post-reach: n = 3604 trials, Saccade: n = 8603 trials. All error bars show mean ± SEM.

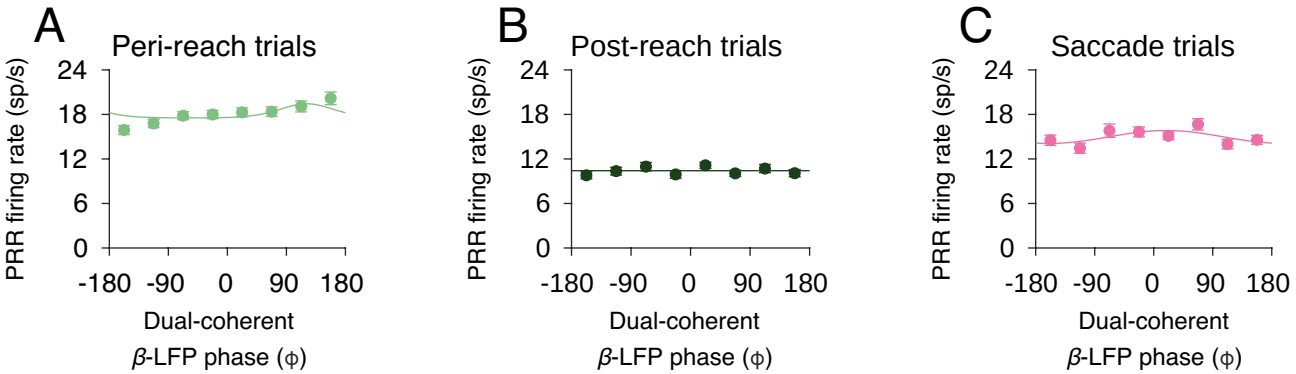

Extended Data Fig. 10 | Dual-coherent *β*-LFP phase is weakly correlated with PRR firing rate. a–**c**, PRR firing rate and a function of dual-coherent *β*-LFP phase for each peri-reach (**a**), post-reach (**b**), and saccade (**c**) trials. Solid lines present changes in SSRT fitted by von Mises function (Peri-reach: p = 0, preferred phase = −121°. Post-reach: p = 0.23. Saccade: p = 0, preferred phase = 19°, likelihood-ratio test). Peri-reach: n = 4814 trials, Post-reach: n = 2116 trials, Saccade: n = 3583 trials (same dataset shown in Figs. 2, 3). All error bars show mean ± SEM.

nature portfolio

Corresponding author(s): Pesaran

Last updated by author(s): Mar 2, 2022

Reporting Summary

Nature Portfolio wishes to improve the reproducibility of the work that we publish. This form provides structure for consistency and transparency in reporting. For further information on Nature Portfolio policies, see our Editorial Policies and the Editorial Policy Checklist.

Statistics

For all statistical analyses, confirm that the following items are present in the figure legend, table legend, main text, or Methods section.

n/a	Confirmed	
☐	☒	The exact sample size (*n*) for each experimental group/condition, given as a discrete number and unit of measurement
☐	☒	A statement on whether measurements were taken from distinct samples or whether the same sample was measured repeatedly
☐	☒	The statistical test(s) used AND whether they are one- or two-sided *Only common tests should be described solely by name; describe more complex techniques in the Methods section.*
☐	☒	A description of all covariates tested
☐	☒	A description of any assumptions or corrections, such as tests of normality and adjustment for multiple comparisons
☐	☒	A full description of the statistical parameters including central tendency (e.g. means) or other basic estimates (e.g. regression coefficient) AND variation (e.g. standard deviation) or associated estimates of uncertainty (e.g. confidence intervals)
☐	☒	For null hypothesis testing, the test statistic (e.g. *F*, *t*, *r*) with confidence intervals, effect sizes, degrees of freedom and *P* value noted *Give P values as exact values whenever suitable.*
☒	☐	For Bayesian analysis, information on the choice of priors and Markov chain Monte Carlo settings
☒	☐	For hierarchical and complex designs, identification of the appropriate level for tests and full reporting of outcomes
☐	☒	Estimates of effect sizes (e.g. Cohen's *d*, Pearson's *r*), indicating how they were calculated

Our web collection on statistics for biologists contains articles on many of the points above.

Software and code

Policy information about availability of computer code

Data collection	Eye position was monitored with a video-based eye tracker (I-Scan). Visual stimuli were generated using an array of tristate light-emitting diodes (LEDs, Kingbright, USA) situated directly behind a touch screen (ELO Touchsystems). The visual stimuli were controlled via custom LabVIEW (8.5, National Instruments) software executed on a real-time embedded system (NI PXI-8184, National Instruments). Neural recordings were made using multiple-electrode microdrives (Double MT, Alpha Omega). Spiking and LFP activity were recorded with glass-coated tungsten electrodes (Alpha Omega) with impedance 0.7–1.4 MΩ measured at 1 kHz (Bak Electronics). Neural signals were amplified (×10,000; TDT Electronics), digitized at 20 kHz with 12 bits/sample (National Instruments), and continuously streamed to disk during the experiment (custom C and Matlab 2019a code) .
Data analysis	Data analysis was performed using custom MATLAB 2019a code. The circular statistics toolbox in Matlab (2019a The Mathworks) was used to perform circular statistical tests (Berens, 2009).

For manuscripts utilizing custom algorithms or software that are central to the research but not yet described in published literature, software must be made available to editors and reviewers. We strongly encourage code deposition in a community repository (e.g. GitHub). See the Nature Portfolio guidelines for submitting code & software for further information.

Data

Policy information about availability of data

All manuscripts must include a data availability statement. This statement should provide the following information, where applicable:

- Accession codes, unique identifiers, or web links for publicly available datasets
- A description of any restrictions on data availability
- For clinical datasets or third party data, please ensure that the statement adheres to our policy

Data availability: The datasets generated during the current study are available at https://github.com/mauhagan/Hagan2022Nature
Code availability: Matlab code for current study are available at https://github.com/mauhagan/Hagan2022Nature

Field-specific reporting

Please select the one below that is the best fit for your research. If you are not sure, read the appropriate sections before making your selection.

☒ Life sciences ☐ Behavioural & social sciences ☐ Ecological, evolutionary & environmental sciences

For a reference copy of the document with all sections, see nature.com/documents/nr-reporting-summary-flat.pdf

Life sciences study design

All studies must disclose on these points even when the disclosure is negative.

Sample size	Sample sizes were based on previous work in the lab (eg Dean et al 2012; Hawellek et al 2016) that determined the necessary sample size for determining statistical significance to estimate the expected number of trials per day the subjects would complete, and how many trials were necessary to have the power to detect behavioral and neural effects.
Data exclusions	Cells were isolated and mapped for spatial selectivity using a visually-guided, center-out, delayed saccade task to eight possible target locations, as described above. If the neuron appeared to show spatial selectivity, the double-step tasks were run, including all of the test conditions described above. Each cell was recorded for a minimum of 10 trials in the preferred direction for each task condition (peri-reach, post-reach and saccade trials). If the cell met these two criteria (spatial selectivity in a center-out task and minimum number of trials), the cell was included in the database. Importantly, there were no inclusion or exclusion criteria based on neural responses in either of the double-step tasks.
Replication	Results were replicated across two subjects. Furthermore, the subjects were counter-balanced for cortical hemisphere (M1 - recordings were made in the left posterior parietal cortex; M2 - recordings were made in the right posterior parietal cortex). Replication was successful.
Randomization	Each monkey first performed a center-out saccade task to map the spatial response fields of neurons. In this task, trials contained saccade targets one of eight different locations and were randomly interleaved. Each monkey then performed the reach-and-saccade double-step task, RS trials, or the saccade-saccade double-step task, SS trials, to study gaze-anchoring in a manner that was consistent with natural behaviour. On a subset of catch trials (percent of trials: 1028, meanSTD), subjects performed only the first step of the double-step tasks with no second target to suppress anticipation. All RS, SS and catch trial conditions were randomly interleaved.
Blinding	Subjects were not allocated to different groups, therefore blinding is not relevant for this study.

Reporting for specific materials, systems and methods

We require information from authors about some types of materials, experimental systems and methods used in many studies. Here, indicate whether each material, system or method listed is relevant to your study. If you are not sure if a list item applies to your research, read the appropriate section before selecting a response.

Materials & experimental systems

n/a	Involved in the study
☒	☐ Antibodies
☒	☐ Eukaryotic cell lines
☒	☐ Palaeontology and archaeology
☐	☒ Animals and other organisms
☒	☐ Human research participants
☒	☐ Clinical data
☒	☐ Dual use research of concern

Methods

n/a	Involved in the study
☒	☐ ChIP-seq
☒	☐ Flow cytometry
☐	☒ MRI-based neuroimaging

Animals and other organisms

Policy information about studies involving animals; ARRIVE guidelines recommended for reporting animal research

Laboratory animals	Two male rhesus monkeys (Macaca mulatta) participated in the experiments (Monkey 1, 9.5 kg, age 6 years and Monkey 2, 6.5 kg, age 9 years).
Wild animals	No wild animals were used in this study
Field-collected samples	No field collected samples were used in this study.
Ethics oversight	All surgical and animal care procedures were done in accordance with National Institute of Health guidelines and were approved by the New York University Animal Care and Use Committee.

Note that full information on the approval of the study protocol must also be provided in the manuscript.

Magnetic resonance imaging

Experimental design

Design type	Anatomical MRI
Design specifications	Anatomical MRI was performed for the purpose of localizing the recording chamber over the posterior parietal cortex.
Behavioral performance measures	Animals were anesthetized for the duration of the scan.

Acquisition

Imaging type(s)	Structural MRI
Field strength	3T
Sequence & imaging parameters	2 pairs of forward/reverse MPRAGE T1-weighted scans with 0.5mm isotropic resolution covering the whole head and extending to include fiducial markers necessary for surgical co-registration using the Brainsight system from Rogue Research (v1.7.10 Canada)
Area of acquisition	Whole brain scan

Diffusion MRI ☐ Used ☐ Not used

Preprocessing

Preprocessing software	Scans were preprocessed using FSL v5 to register and average images across scans with the commands fslmaths and flirt. The resulting volume was then loaded into the Brainsight software suite v1.7.10 where they were further preprocessed to localize MR-visible electrode registration features. We did not preprocess the images to extract the brain or skull.
Normalization	Neuroimaging data were not normalized because they were used only for anatomical co-registraton of the recording electrodes and the sulcal recording sites in the posterior parietal cortex.
Normalization template	The data were not normalized.
Noise and artifact removal	We did not need to remove artifacts from the structural MRI because at the time of imaging animals were implanted with MR-compatible materials (ceramic screws and chambers manufactured from ultem and peek).
Volume censoring	We did not perform volume censoring.

Statistical modeling & inference

Model type and settings	N/A
Effect(s) tested	N/A

Specify type of analysis: ☒ Whole brain ☐ ROI-based ☐ Both

Statistic type for inference (See Eklund et al. 2016)	N/A
Correction	N/A

Models & analysis

n/a	Involved in the study
☒	☐ Functional and/or effective connectivity
☒	☐ Graph analysis
☐	☒ Multivariate modeling or predictive analysis

Multivariate modeling and predictive analysis

We created a model to predict LIP firing rates based on PRR inputs. Model parameters were estimated using PRR firing rates and the behavioral data using maximum likelihood. Importantly, LIP spike rates were not used in fitting either the inhibitory gain function or the modulation state function. The inhibitory channel model only depends on LIP spiking activity for a base rate starting point for the model on each trial. We characterized the performance of the model by calculating the mean squared error (MSE) between the observed LIP firing rate on each trial and the predicted LIP firing rate on each trial according to the model. For comparison, we also calculated the MSE for an input gain function only model, which did not include the modulation state function, a modulation state only model, which did not include the inhibitory input gain function, and a linear regression model. The linear regression, unlike the other models, was fit using the observed LIP firing rates on each trial.